ROYAL SOCIETY
OF CHEMISTRY

PAPER

Check for updates

One-pot green synthesis of Ag/Ni/Fe₃O₄-activated carbon beads for recyclable photo-Fenton antibiotic removal and antibacterial action: mechanistic study and optimization†

Viet Hung Hoang,[a] Thi Ngoc Bich Phan,[b] Van Thanh Nguyen,[a] Thi Thao Le,[a] Minh Hieu Do,[a] Van Tuynh Luu,[a] Vy Anh Tran,[c] Van-Dat Doan ⓘD *[b] and Van Thuan Le ⓘD *[de]

A one-pot green synthesis approach was developed to fabricate Ag/Ni/Fe₃O₄-activated carbon beads (Ag/Ni/MACB) using *Brucea javanica* as a natural carbon precursor. Unlike conventional powdered catalysts, these millimeter-sized porous beads enable easy recovery and reusability, addressing a key limitation in heterogeneous Fenton systems. The Fe₃O₄ component facilitated Fenton-like reactions, while Ni and Ag nanoparticles synergistically enhanced electron transfer and visible-light absorption, significantly boosting photo-Fenton efficiency. The catalyst achieved 96.78% enrofloxacin (ENR) degradation under optimized conditions, with radical scavenger experiments confirming that ˙OH and ˙O₂⁻ were the dominant reactive species. Comprehensive characterization (XRD, SEM, TEM, BET, VSM, and FTIR) verified the uniform dispersion of Fe₃O₄, Ni, and Ag nanoparticles (10–50 nm) within the carbon matrix, ensuring structural stability and catalytic efficiency. The incorporation of Ag not only improved light absorption but also imparted strong antibacterial properties, effectively inhibiting *Escherichia coli* and *Staphylococcus aureus*. This dual functionality allows Ag/Ni/MACB to simultaneously degrade organic pollutants and eliminate bacterial contamination, demonstrating self-cleaning capability. The catalyst retained 83.61% efficiency after five cycles with negligible metal leaching, highlighting its long-term stability and recyclability. Additionally, the degradation pathway of ENR was elucidated, providing deeper insights into the reaction mechanism. By integrating sustainable material design, enhanced photocatalytic properties, and antibacterial action, Ag/Ni/MACB serves as a versatile and cost-effective solution for wastewater treatment, offering simultaneous pollutant degradation and microbial disinfection in a single step.

1. Introduction

The increasing presence of antibiotics in aquatic environments has become a pressing environmental issue, contributing to the spread of antibiotic resistance and disrupting microbial ecosystems.[1,2] Enrofloxacin (ENR), a widely used fluoroquinolone

aInstitute of Tropical Durability, Vietnam-Russia Tropical Science and Technology Research Center, 63 Nguyen Van Huyen, Ha Noi City, 100000, Vietnam

bFaculty of Chemical Engineering, Industrial University of Ho Chi Minh City, Ho Chi Minh City, 700000, Vietnam. E-mail: doanvandat@iuh.edu.vn

cDepartment of Material Science, Institute of Applied Technology and Sustainable Development, Nguyen Tat Thanh University, Ho Chi Minh City, 700000, Vietnam

dCenter for Advanced Chemistry, Institute of Research & Development, Duy Tan University, 03 Quang Trung, Da Nang City, 550000, Vietnam. E-mail: levanthuan3@duytan.edu.vn

eFaculty of Natural Sciences, Duy Tan University, 03 Quang Trung, Da Nang City, 550000, Vietnam

antibiotic in veterinary medicine, is frequently detected in wastewater due to its extensive use and low biodegradability. Residual ENR in water sources poses severe risks to aquatic life and human health, emphasizing the urgent need for effective removal strategies.[3] Traditional wastewater treatment methods, such as adsorption, membrane filtration, and biodegradation, have shown limited efficiency in completely degrading ENR. Adsorption merely transfers pollutants without breaking them down, leading to secondary contamination. Membrane filtration can effectively separate ENR from water but suffers from high operational costs, membrane fouling, and the need for frequent replacement. Biodegradation, while environmentally friendly, is often slow and ineffective against fluoroquinolones due to their stable molecular structure and resistance to microbial degradation.[4] These limitations highlight the necessity for more efficient and sustainable treatment technologies.

Advanced oxidation processes (AOPs) have been widely studied for their effectiveness in breaking down persistent

Paper

organic pollutants into non-toxic byproducts. Among these, the photo-Fenton process stands out due to its capability to produce highly reactive hydroxyl radicals ($^{\bullet}$OH), which facilitate the degradation of complex contaminants such as ENR.[5] Unlike conventional Fenton reactions, the photo-Fenton process utilizes light energy to accelerate Fe^{2+} regeneration, enhancing the production of $^{\bullet}$OH and improving degradation efficiency.[6] However, homogeneous Fenton systems suffer from narrow pH applicability, iron sludge generation, and catalyst loss, limiting their large-scale application.[7] To overcome these challenges, the development of heterogeneous, recyclable, and cost-effective photo-Fenton catalysts is essential for improving process sustainability and efficiency.

Recent studies have explored various catalysts for the photo-Fenton process, with particular emphasis on Fe_3O_4-based materials due to their intrinsic catalytic activity in Fenton-like reactions.[8–10] This is attributed to their ability to facilitate the Fe^{2+}/Fe^{3+} redox cycle, which is essential for the continuous generation of highly reactive hydroxyl radicals. Additionally, their magnetic properties enable easy separation and reuse, making them promising candidates for wastewater treatment applications.[11] To further enhance catalytic performance, researchers have investigated the incorporation of Ni or Ag nanoparticles, which improve electron transfer efficiency and light absorption.[12,13] Moreover, Ag exhibits strong antibacterial properties, helping to mitigate microbial interference in wastewater treatment and further enhancing process efficiency. Additionally, carbon-based materials such as activated carbon (AC), graphene, and biochar have gained attention as catalyst supports due to their high surface area, stability, and ability to promote the dispersion of active sites.[4,14–16] Despite these advancements, several challenges remain. Most existing catalysts are in powdered form, making recovery and reuse difficult, thus limiting practical application. Furthermore, many synthesis methods involve complex procedures and costly precursors, reducing scalability for real-world wastewater treatment. Additionally, while recent studies report promising degradation efficiencies, the reaction mechanisms in heterogeneous photo-Fenton systems remain insufficiently explored, particularly regarding the synergistic effects between different catalytic components. Addressing these limitations is crucial for developing an efficient, cost-effective, and recyclable catalyst for sustainable wastewater treatment.

To address the aforementioned limitations of existing photo-Fenton catalysts, this study proposes the one-pot green synthesis of $Ag/Ni/Fe_3O_4$-activated carbon beads (Ag/Ni/MACB) using *Brucea javanica* as a natural precursor and structural template. Unlike conventional plant-mediated syntheses, which rely on plant extracts as reducing agents, *B. javanica* seeds are directly utilized due to their naturally occurring bead-like morphology. This intrinsic structure provides a ready-made template for the formation of ACB, eliminating the need for additional processing steps. Moreover, the seeds possess a porous architecture, which enhances the adsorption and controlled deposition of metal ions during the impregnation step. Upon thermal treatment, the seeds are converted into AC while simultaneously facilitating the *in situ* reduction of metal

ions, leading to the formation of Fe_3O_4, Ni, and Ag nanoparticles embedded within the carbon matrix. This integrated approach not only simplifies catalyst fabrication but also enhances material sustainability by eliminating the need for external reducing agents and synthetic carbon precursors. *B. javanica* is widely available in Vietnam, growing abundantly in the wild and producing fruit year-round. Its accessibility, renewable nature, and established medicinal applications demonstrate its non-toxic properties, making it a promising candidate for sustainable material development and an eco-friendly alternative to conventional carbon precursors.[17] Furthermore, the formation of Ag/Ni/MACB leverages the synergistic effects of Fe_3O_4, Ni, and Ag to enhance electron transfer efficiency, boost light absorption under visible-light irradiation, and introduce antimicrobial properties, further contributing to water purification. Additionally, the ACB structure provides a robust support system, ensuring mechanical stability, easy separation from treated water, and improved reusability—key factors for practical wastewater treatment applications.

The synthesized Ag/Ni/MACB catalyst was systematically evaluated for its efficiency in the photo-Fenton degradation of ENR under varying reaction conditions. A detailed investigation of the degradation mechanism was conducted through spectroscopic analysis and radical scavenger experiments to elucidate the reactive species involved. Furthermore, key reaction parameters were optimized to achieve maximum degradation efficiency, ensuring the catalyst's practical applicability. Beyond its catalytic performance, the antibacterial properties and reusability of Ag/Ni/MACB were also assessed, highlighting its potential for long-term deployment in wastewater treatment. By integrating a naturally derived, renewable, and non-toxic carbon source with advanced catalytic engineering, this work presents a sustainable, multifunctional, and highly efficient photo-Fenton catalyst for environmental remediation.

2. Materials and methods

2.1. Materials

Iron(III) nitrate nonahydrate ($Fe(NO_3)_3 \cdot 9H_2O$, $\geq$98.0%), nickel(II) nitrate hexahydrate ($Ni(NO_3)_2 \cdot 6H_2O$, >99.0%), and silver nitrate ($AgNO_3$, $\geq$99.8%) were purchased from Acros Organics (Belgium) and used as precursors for catalyst synthesis. Enrofloxacin ($\geq$99.0%) was obtained from Sigma-Aldrich (Singapore) for degradation experiments. For radical scavenging tests, disodium ethylenediaminetetraacetate dihydrate (Na_2-EDTA$\cdot 2H_2O$, $\geq$99.0%), potassium persulfate ($K_2S_2O_8$, $\geq$99.0%), *p*-benzoquinone (*p*-BQ, $\geq$98.0%), and isopropanol (IPA, $\geq$99.5%) were acquired from Sigma-Aldrich (Singapore). Hydrochloric acid (HCl, 37.0%), sodium hydroxide (NaOH, $\geq$98.0%), and ethanol (C_2H_5OH, $\geq$99.7%) were purchased from Xilong Scientific (China) and used for pH adjustment and sample washing. Additionally, analytical-grade reagents including sodium bicarbonate ($NaHCO_3$, $\geq$99.7%), sodium dihydrogen phosphate (NaH_2PO_4, $\geq$99.0%), sodium chloride (NaCl, $\geq$99.5%), sodium nitrate ($NaNO_3$, $\geq$99.0%), sodium sulfate (Na_2SO_4, $\geq$99.0%), calcium chloride dihydrate

(CaCl$_2$·2H$_2$O, ≥99.0%), and magnesium chloride hexahydrate (MgCl$_2$·6H$_2$O, ≥98.0%) were obtained from Xilong Scientific (China) and used to investigate the effect of coexisting inorganic ions in degradation experiments. Mature *Brucea javanica* seeds were collected from Da Nang, Vietnam. The harvested seeds were manually depulped, thoroughly washed with distilled water, and dried at 60 °C before use as a natural carbon precursor and structural template in catalyst synthesis.

2.2. Synthesis of Ag/Ni/MACB

The synthesis of Ag/Ni/MACB followed the procedure outlined in Scheme 1. Specifically, calculated amounts of Fe(NO$_3$)$_3$·9H$_2$O, Ni(NO$_3$)$_2$·6H$_2$O, and AgNO$_3$ were dissolved in 50 mL of distilled water under constant stirring to form a homogeneous precursor solution. Subsequently, 5 g of *B. javanica* seeds were introduced into the solution, and the mixture was stirred at 65 °C for 24 h to facilitate the impregnation of metal ions onto the seed structure. After impregnation, the metal-loaded seeds were transferred into a crucible with a sealed lid and subjected to pyrolysis at 500 °C for 1 h. The obtained product was sequentially washed with 50% ethanol and distilled water to remove residual impurities and then dried at 60 °C overnight. The Ag/Ni/MACB catalysts were synthesized with varying Fe^{3+} : Ni^{2+} : Ag$^+$ molar ratios, including 2 : 1 : 0.125, 2 : 1 : 0.25, 2 : 1 : 0.5, 2 : 1 : 0.75, and 2 : 1 : 1. Additionally, control samples, including Fe$_3$O$_4$/ACB (MACB), Ni/ACB, Ag/ACB, and Ni/MACB, were prepared following the same procedure, except that the respective metal precursors were omitted.

2.3. Characterization of catalysts

The synthesized catalysts were systematically characterized using various analytical techniques to gain insights into their physicochemical properties. The surface morphology and microstructural features were examined using field emission scanning electron microscopy (FE-SEM) on a Hitachi S-4800 microscope (Japan). The elemental composition and metal distribution were further analyzed using an EDX X-ray Micro Analyzer H-7593 (Horiba, Japan) attached to the FE-SEM system. High-resolution transmission electron microscopy (HR-TEM) was conducted using a JEM 2100 instrument (Japan) to provide detailed information on the size, dispersion, and interface characteristics of the nanostructures. The crystalline

phase identification was carried out by X-ray diffraction (XRD) on a Shimadzu XRD-6100 diffractometer, employing Cu Kα radiation ($\lambda = 1.5406$ Å). The optical properties of the catalysts were explored through photoluminescence (PL) measurements using a FL FluoroMax Plus-C instrument (Horiba, Japan) and diffuse reflectance UV-Vis spectroscopy (UV-Vis DRS) with a Shimadzu UV-2401 PC spectrophotometer (Japan). The textural properties, including specific surface area and porosity, were determined by Brunauer–Emmett–Teller (BET) analysis using a NOVA 1200e surface area analyzer (Quantachrome Instruments, USA). Before measurements, the samples were degassed at 300 °C for 5 h under vacuum. The nitrogen adsorption–desorption isotherms were recorded at 77.3 K to evaluate pore size distribution and total pore volume. Fourier-transform infrared (FT-IR) spectroscopy was conducted using a Tensor 27 spectrometer (Bruker, Germany) to identify surface functional groups and chemical interactions. The magnetic behavior was evaluated *via* vibrating sample magnetometry (VSM) using a VSM-DMS 880 system (USA) to determine saturation magnetization and coercivity values. Thermal stability and decomposition behavior were examined using thermogravimetric analysis (TGA) on a TA Instruments Trios system. The samples were heated from 25 to 700 °C at a rate of 5 °C min^{-1} under an inert atmosphere to monitor weight loss and material degradation.

2.4. Catalytic experiment

The ENR antibiotic removal efficiency of Ag/Ni/MACB was evaluated through adsorption, photocatalysis, Fenton, and photo-Fenton processes. The experiments were conducted in a specialized photoreactor system equipped with a 500 W halogen lamp, a $\lambda \geq 420$ nm optical filter, a mechanical stirrer, a thermostatic water bath, and a three-necked reaction flask to maintain stable reaction conditions. In a typical photo-Fenton experiment, a predetermined amount of Ag/Ni/Fe$_3$O$_4$–ACB was dispersed in 100 mL of 10 mg L^{-1} ENR solution under continuous stirring in the dark for 1 h to establish adsorption equilibrium. At designated time intervals, 2 mL aliquots were withdrawn, filtered to remove solid particles, and analyzed using UV-Vis spectrophotometry (Cary 60, Agilent, USA) to determine the residual ENR concentration at $\lambda_{max} = 287$ nm. After reaching equilibrium, a calculated amount of H$_2$O$_2$ was
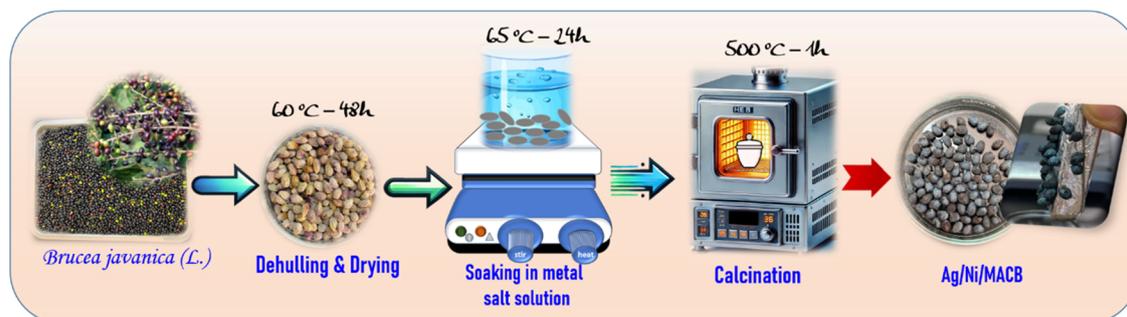
Scheme 1 Schematic illustration of the synthesis process of Ag/Ni/MACB *via* a one-pot green synthesis.

introduced, and the reaction system was exposed to visible light irradiation for 150 min, with sampling every 30 min to monitor the degradation process. The effects of key operational parameters, including initial ENR concentration (5–20 mg L^{-1}), catalyst dosage (6–10 g L^{-1}), pH (3–9), temperature (25–55 °C) and the presence of coexisting inorganic ions, were systematically investigated to determine the optimal reaction conditions.

The degradation efficiency ($R\%$) was calculated based on the ratio of the difference between the initial antibiotic concentration (C_0, mg L^{-1}) and the antibiotic concentration at time t (C_t, mg L^{-1}) to the initial concentration, as expressed in eqn (1).

$$R\ (\%) = \frac{C_0 - C_t}{C_0} \times 100 \tag{1}$$

The extent of mineralization was assessed by monitoring the reduction in Chemical Oxygen Demand (COD) and Total Organic Carbon (TOC). TOC levels were quantified using a Multi N/S 2100S TOC analyzer (Analytik Jena, Germany), while COD was measured through the dichromate oxidation method with a HI839150 COD reactor (Hanna Instruments). The mineralization efficiency was calculated using the following equations:

$$\%\ \text{COD reduction} = \frac{\text{COD}_i - \text{COD}_f}{\text{COD}_i} \times 100 \tag{2}$$

$$\%\ \text{TOC reduction} = \frac{\text{TOC}_i - \text{TOC}_f}{\text{TOC}_f} \times 100 \tag{3}$$

where COD$_i$ and TOC$_i$ represent the initial COD and TOC values, while COD$_f$ and TOC$_f$ correspond to the final values.

The kinetics of ENR degradation were evaluated by fitting the experimental data to zero-order, first-order, and second-order kinetic models, as described in eqn (4)–(6):

$$\text{Zero-order kinetics: } C_t = C_0 - k_0 t \tag{4}$$

$$\text{First-order kinetics: } \ln C_t = \ln C_0 - k_1 t \tag{5}$$

$$\text{Second-order kinetics : } \frac{1}{C_t} = \frac{1}{C_0} + k_2 t \tag{6}$$

where C_0 (mg L^{-1}) and C_t (mg L^{-1}) represent the initial and residual ENR concentrations at time t (min), respectively, and k_0, k_1, and k_2 are the rate constants for zero-order, first-order, and second-order kinetics, respectively. The most suitable kinetic model was determined based on the correlation coefficient (R^2), with the best-fit model providing insight into the reaction mechanism.

2.5. Mechanism insight

To elucidate the underlying reaction mechanism of the photo-Fenton process, radical quenching experiments were performed using specific scavengers at a concentration of 10 mM. Specifically, Na$_2$EDTA·2H$_2$O was used to capture holes (h$^+$), K$_2$S$_2$O$_8$ was employed to scavenge electrons (e$^-$), p-BQ was utilized for superoxide radicals ($^{\bullet}$O$_2^-$), and IPA was applied to quench hydroxyl radicals ($^{\bullet}$OH). The inhibitory effects of these scavengers on ENR degradation were systematically analyzed to identify the predominant reactive species contributing to the degradation process. Additionally, liquid chromatography-mass spectrometry (LC-MS/MS) analysis was conducted to investigate the degradation pathways of ENR in catalytic experiments. The analysis was performed using an HPLC 20 AXL system (Shimadzu) coupled with an ABI 5500 QQQ mass spectrometer (Applied Biosystem). Chromatographic separation was achieved using a C18 column (150 mm × 2.1 mm × 3.5 μm, Agilent) at a column temperature of 30 °C. The mobile phase consisted of water containing 0.1% formic acid and acetonitrile, with a flow rate of 0.4 mL min^{-1}. By identifying the intermediate products, the possible transformation routes of ENR degradation were proposed, providing further insights into its oxidative breakdown under photo-Fenton conditions.

2.6. Stability and reusability

To evaluate the stability and reusability of the Ag/Ni/MACB catalyst, five consecutive degradation cycles were performed. After each cycle, the catalyst was magnetically separated, thoroughly washed with distilled water, and dried before reuse. The degradation efficiency across cycles was compared to assess the long-term catalytic performance. Structural integrity and potential surface modifications of the used catalysts were analyzed using XRD to assess crystallographic stability, SEM to observe morphological changes, and FT-IR to investigate potential functional group variations. Additionally, to evaluate the leaching of metal ions (Fe, Ni, Ag), the filtrates from each reaction cycle were analyzed using inductively coupled plasma mass spectrometry (ICP-MS, Agilent 7700 series, USA).

2.7. Antibacterial activity evaluation

The antibacterial activity of the synthesized materials was assessed against *Escherichia coli* (*E. coli*, ATCC 25922) and *Staphylococcus aureus* (*S. aureus*, ATCC 6538) using the agar well diffusion method. Mueller–Hinton agar plates were inoculated with bacterial suspensions adjusted to 0.5 McFarland standard ($\sim$1.5 × 10^8 CFU mL^{-1}) using a sterile cotton swab. Sterile wells were created in the agar medium, into which individual granules of the synthesized material were placed. Gentamicin (100 ppm) served as the positive control, while sterile distilled water was used as the negative control. The plates were incubated at 37 °C for 24 h, after which the diameter of the inhibition zone (including the well) was measured to evaluate antibacterial efficacy. All experiments were performed in triplicate, and results were expressed as the mean ± standard deviation.

3. Results and discussion

3.1. Synthesis and characterization of the catalyst

3.1.1. Formation mechanism of Ag/Ni/MACB and phase composition analysis. The Ag/Ni/MACB composite was synthesized *via* a pyrolysis-assisted metal loading approach, where *B. javanica* seeds served as both a bio-template and a carbon source. The proposed formation mechanism of the Ag/Ni/MACB composite is illustrated in Fig. 1a. Initially, metal ions (Ag$^+$, Ni^{2+}, and Fe^{3+}) are adsorbed onto the surface of *B. javanica* seeds
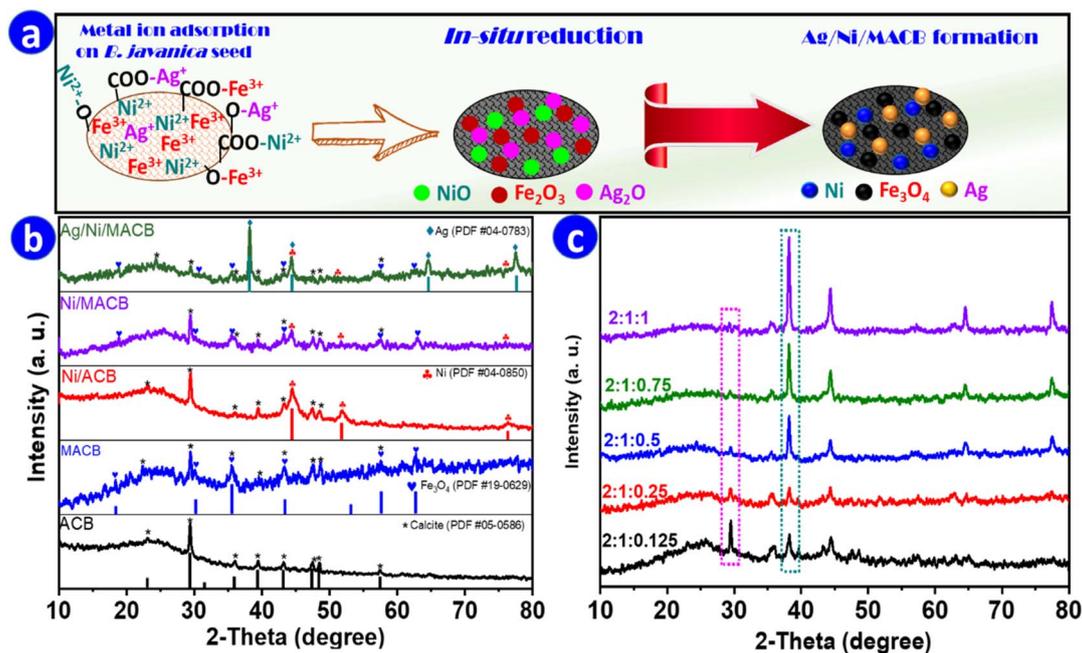
Fig. 1 (a) Proposed formation mechanism of the Ag/Ni/MACB catalyst, (b) XRD patterns of different samples, including ACB, MACB, Ni/ACB, Ni/MACB, and Ag/Ni/MACB, (c) XRD patterns of Ag/Ni/MACB with varying Ag contents.

through interactions with carboxyl (–COO⁻) and hydroxyl (–OH) functional groups. This adsorption process involves coordination between metal ions (Fe^{3+}, Ni^{2+}, and Ag^+) and functional groups such as carboxyl (–COO⁻) and hydroxyl (–OH), leading to the formation of metal–organic complexes, as described in eqn (7):

$$\equiv + Fe^{3+}/Ni^{2+}/Ag^+ \rightarrow \equiv Fe/Ni/Ag \quad (7)$$
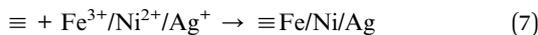
where "$\equiv$" represents the active functional groups (*e.g.*, carboxyl ($RCOO^-$) and hydroxyl (RO^-)) on the surface of *B. javanica* seeds, which act as binding sites for metal ions.

Upon pyrolysis under an oxygen-deficient atmosphere, the *B. javanica* seeds undergo carbonization, transforming into ACB. Simultaneously, the metal–organic complexes decompose to form metal oxides, as shown in eqn (8):

$$\equiv Fe/Ni/Ag \xrightarrow{t^0} Ag_2O/NiO/Fe_2O_3/ACB$$
$$+ CO_2/CO + \text{other gases} \quad (8)$$
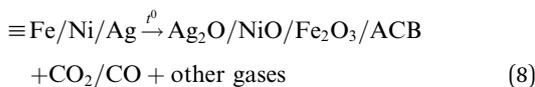
At elevated temperatures, the carbon matrix of ACB, along with carbon monoxide (CO) generated during pyrolysis, acts as a reducing agent, facilitating the reduction of Fe_2O_3, NiO, and Ag_2O into Fe_3O_4, metallic Ni, and Ag nanoparticles, respectively, as described in eqn (9):

$$Ag_2O/NiO/Fe_2O_3/ACB + C/CO \xrightarrow{t^0}$$
$$Ag/Ni/Fe_3O_4/ACB + CO/CO_2 \quad (9)$$
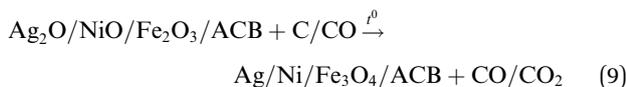
The final Ag/Ni/MACB composite consists of well-dispersed Ag and Ni nanoparticles supported on a Fe_3O_4-modified carbonaceous matrix. This structure is expected to enhance catalytic and antibacterial performance due to the synergistic effects of the different components. Notably, the formation of metal and metal oxide nanoparticles on carbon-based supports under pyrolysis conditions has been extensively reported in previous studies, further supporting the validity of the proposed mechanism.[8,18,19]

To validate the proposed formation mechanism and confirm the phase composition of the synthesized Ag/Ni/MACB composite, XRD analysis was conducted, as presented in Fig. 1b and c. The ACB sample, obtained by direct pyrolysis of biomass-derived precursors without metal salt impregnation, exhibits a broad diffraction peak at 14–22°, characteristic of amorphous carbon. Additionally, diffraction peaks at $2\theta \approx$ 23.1°, 29.4°, 35.9°, 39.4°, 43.1°, 47.5°, and 48.5° correspond to $CaCO_3$ (calcite phase, PDF no. 05-0586), likely originating from inherent mineral components within the biomass that remained stable under pyrolysis conditions.[20] For the MACB sample, where the precursor was first immersed in an Fe^{3+} solution before pyrolysis, the XRD pattern reveals characteristic peaks at $2\theta \approx$ 30.1°, 35.5°, 43.2°, 57.1°, and 62.6°, corresponding to the (220), (311), (400), (511), and (440) planes of Fe_3O_4 (PDF no. 19-0629).[21] This confirms the *in situ* formation of Fe_3O_4 within the carbon matrix. Similarly, in the Ni/ACB sample, where the precursor was immersed in a Ni^{2+} solution before pyrolysis, three distinct peaks at $2\theta \approx$ 44.5°, 51.8°, and 76.4° are observed, corresponding to the (111), (200), and (220) planes of metallic Ni (PDF no. 04-0850), verifying the successful incorporation of Ni.[22] For the Ni/MACB sample, which was impregnated with both Ni^{2+} and Fe^{3+} prior to pyrolysis, the XRD pattern displays diffraction peaks corresponding to both Fe_3O_4 and Ni, indicating a well-integrated hybrid structure within the

Paper

composite. Finally, in the Ag/Ni/MACB sample, new diffraction peaks appear at $2\theta \approx 38.1°$, $44.3°$, and $64.5°$, corresponding to the (111), (200), and (220) reflections of metallic Ag (PDF no. 04-0783), confirming the successful deposition of silver onto the composite.[23]

To further elucidate the impact of varying Ag^+ concentrations on the composite structure, XRD analysis was performed for Ag/Ni/MACB samples synthesized at different $Fe^{3+}:Ni^{2+}:Ag^+$ molar ratios, including $2:1:0.125$, $2:1:0.25$, $2:1:0.5$, $2:1:0.75$, and $2:1:1$ (Fig. 1c). In this series, the $Fe^{3+}:Ni^{2+}$ ratio was maintained constant to ensure that Fe_3O_4 remained the dominant phase, as its superparamagnetic properties facilitate catalyst recovery and its Fenton-like activity enhances catalytic performance. Meanwhile, the Ag^+ concentration was varied due to its high cost, ensuring an optimal balance between catalytic enhancement and economic feasibility. The XRD patterns reveal a characteristic peak at $29.4°$, corresponding to $CaCO_3$, which remains present across all samples. Notably, the intensity of this peak decreases with increasing Ag^+ concentration. This suggests a possible ion exchange mechanism, where Ag^+ competes with Ca^{2+} on the composite surface, leading to partial replacement of Ca^{2+}. A similar trend is observed for the diffraction peaks of Ag at $38.1°$, $44.3°$, and $64.5°$, which become more pronounced with higher Ag^+ concentrations, confirming the successful incorporation of Ag into the composite. However, an exception is noted at the $2:1:0.25$ ratio, where the intensity of the $44.3°$ peak is slightly lower than that of the $2:1:0.125$ sample. This deviation may be attributed to localized variations in Ag dispersion and crystallinity at this intermediate concentration. Specifically, partial aggregation of AgNPs or their embedding within the composite matrix could suppress the diffraction intensity. Such fluctuations are not uncommon in multicomponent systems, especially during early stages of Ag incorporation, and may reflect transient structural reorganization prior to more uniform crystallization at higher Ag^+ concentrations. These findings indicate that the gradual introduction of Ag^+ influences both the phase composition and structural properties of the material, highlighting the interplay between metal ion exchange and composite formation. Moreover, the presence of $CaCO_3$ is not detrimental, as it is an environmentally benign component. Additionally, its content can be further minimized by increasing the concentration of metal ions, providing a potential route to further refine the composite properties if necessary.

3.1.2. Morphological and elemental analysis (SEM, EDX, TEM). The morphological characteristics and elemental distribution of Ag/Ni/MACB (0.5) ($Fe^{3+}:Ni^{2+}:Ag^+ = 2:1:0.5$) were investigated using SEM, EDX, and TEM analyses, as presented in Fig. 2. This composition was selected for detailed characterization due to its superior photocatalytic performance compared to other synthesized ratios (ranging from $2:1:0.125$ to $2:1:1$). The synthesized Ag/Ni/MACB particles exhibited a spherical morphology with an average diameter of 4.06 ± 0.06 mm and a length of 6.61 ± 0.25 mm, as determined from the mean values of ten randomly selected particles. The measurements shown in Fig. 2a and b correspond to an individual particle, confirming consistency in size distribution.

The cross-sectional SEM image (Fig. 2c) reveals a well-defined and uniformly porous internal structure, which is further emphasized in the high-magnification image (Fig. 2d), illustrating an interconnected porous network. This intrinsic porosity is expected to enhance mass transport properties and facilitate interactions between the active sites and reactants, making the material highly suitable for catalytic or adsorption applications. A closer examination of the subsurface region near the outer layer (Fig. 2e) indicates the presence of embedded metallic and metal oxide nanoparticles within the porous matrix. This distribution suggests that metal ions may have infiltrated beneath the surface layer *via* an adsorption–diffusion mechanism, leading to uniform incorporation throughout the material. The outer surface morphology (Fig. 2f) further confirms the presence of well-dispersed metal and metal oxide nanoparticles, highlighting their homogeneous distribution. Such a structure is beneficial for ensuring stable catalytic performance and enhancing the magnetic properties of the composite.

The elemental composition of Ag/Ni/MACB was confirmed by EDX analysis (Fig. 2g), revealing the presence of C (58.26 ± 1.62 wt%), O (16.46 ± 0.98 wt%), Fe (14.60 ± 0.81 wt%), Ni (7.81 ± 1.62 wt%), and Ag (2.87 ± 1.33 wt%), aligning well with the expected material composition. Elemental mapping further demonstrates a uniform distribution of these elements across the ACB surface, reinforcing the successful integration of Ag, Ni, and Fe within the carbon-based framework.

Fig. 3 presents the TEM analysis of the Ag/Ni/MACB composite. Fig. 3a shows the distribution of nanoparticles with diverse shapes and sizes (ranging from 10 to 50 nm) on the carbon matrix (appearing as a diffuse background). The nanoparticles are well dispersed across the matrix, confirming their successful incorporation during synthesis. Fig. 3b and c provide high-magnification images of selected nanoparticles, revealing distinct structural characteristics. The observed contrast variations indicate differences in electron density, supporting the presence of multiple metal phases (Ag, Ni, and Fe_3O_4) within the composite. To further confirm the structural identity of these nanoparticles, high-resolution TEM images were analyzed using ImageJ software to determine the interplanar spacing (d-spacing) values. Fig. 3d exhibits an interplanar spacing of 0.24 nm, corresponding to the (111) plane of metallic Ag.[24] Fig. 3e displays a lattice spacing of 0.48 nm, which matches the (111) plane of Fe_3O_4.[25] Meanwhile, Fig. 3f reveals a spacing of 0.21 nm, attributed to the (111) plane of Ni.[26] These values are consistent with reference data, further validating the successful formation of Ag, Ni, and Fe_3O_4 phases in the composite. The combination of uniform nanoparticle dispersion, well-defined crystalline structures, and verified interplanar spacings suggests that the Ag/Ni/MACB composite possesses a robust hierarchical structure, which is crucial for enhancing its functional properties in catalytic applications.

3.1.3. Surface functional groups analysis (FTIR). The surface functional groups of ACB, MACB, Ni/MACB, and Ag/Ni/MACB were analyzed using FTIR spectroscopy, with the corresponding spectra presented in Fig. 4a. The FTIR peak positions and functional group assignments are summarized in Table
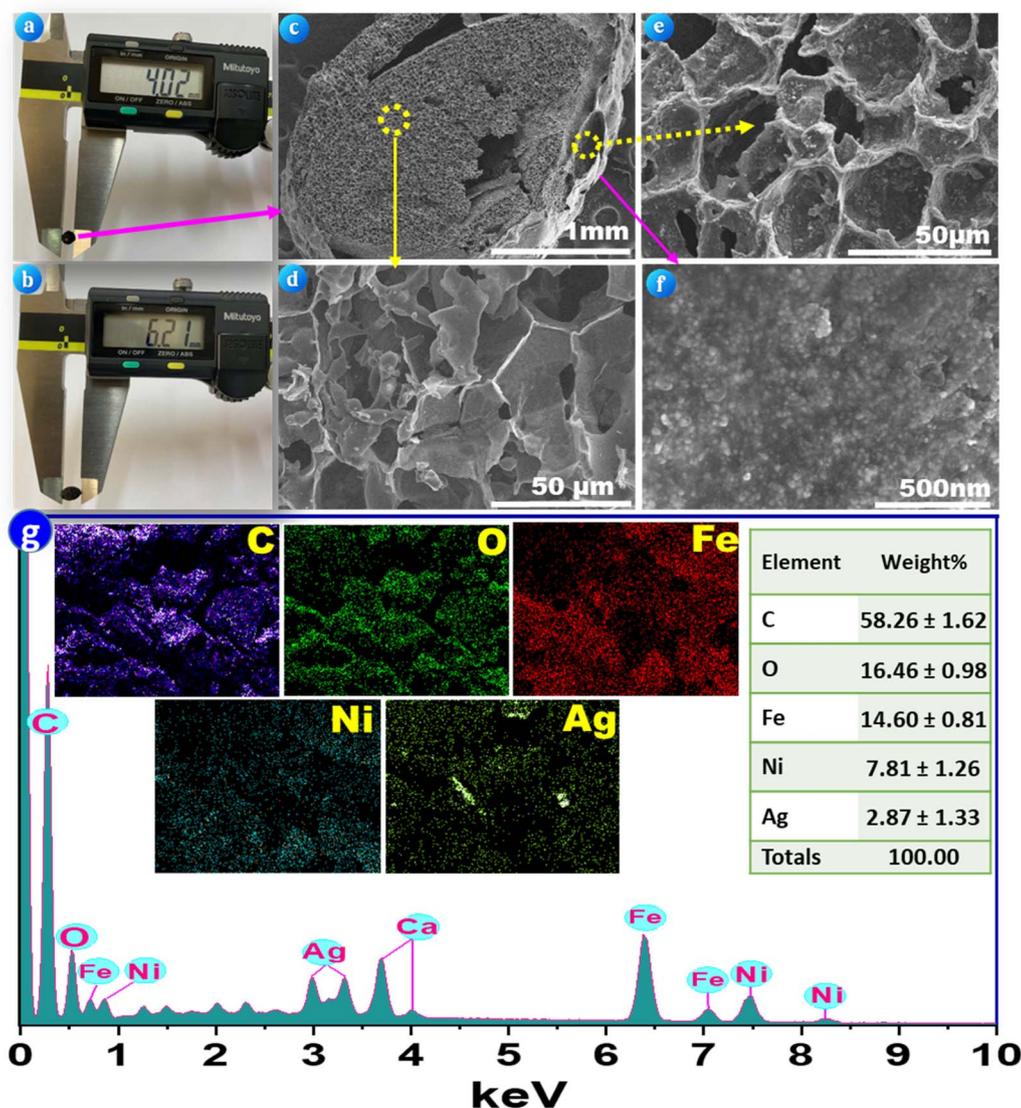
Fig. 2 (a) Optical image showing the measured diameter of the Ag/Ni/MACB; (b) optical image showing the measured length of the Ag/Ni/MACB; (c) SEM image of the cross-section of the Ag/Ni/MACB; (d) high-magnification SEM image of the internal structure within the cross-section, revealing a porous network; (e) high-magnification SEM image of the subsurface region near the outer layer, showing embedded metal and metal oxide nanoparticles; (f) SEM image of the outer surface of the Ag/Ni/MACB, where metal and metal oxide nanoparticles are clearly visible; (g) EDX spectrum of Ag/Ni/MACB, with the inset showing elemental composition (wt%) and elemental mapping images of C, O, Fe, Ni, and Ag.

S1.† A broad band at 3730–3610 cm^{-1} corresponds to hydroxyl (–OH) stretching vibrations, indicating adsorbed water and surface hydroxyls. The peak at 3198 cm^{-1} is attributed to N–H stretching, while bands at 2958–2885 cm^{-1} correspond to C–H stretching vibrations of alkyl groups. The presence of sulfur-containing functional groups is suggested by peaks in the 2723–2581 cm^{-1} range, attributed to thiol (–SH) stretching. A strong peak at ~1745 cm^{-1} corresponds to C=O stretching, likely from ketones or esters. Additional peaks at 1456 and 1375 cm^{-1} are assigned to C–H bending in methylene and methyl groups, while those at 1300 cm^{-1} and 1255 cm^{-1} indicate C–O stretching and C–O–C asymmetric stretching, suggesting ester and ether functionalities.[27] Peaks at 1165 and 1100 cm^{-1} confirm the presence of aliphatic ethers and

alcohols, whereas the band at 1046 cm^{-1} is attributed to polysaccharide-related C–O–C stretching. The 998 and 973 cm^{-1} bands correspond to C=C bending in aromatic rings, and the peaks at 840–808 cm^{-1} are associated with aromatic C–H out-of-plane bending. The absorption band at 570 cm^{-1} confirms Fe–O stretching, indicating Fe$_3$O$_4$ in Ni/MACB and Ag/Ni/MACB, while the ~452 cm^{-1} peak suggests Ca–O stretching.[28]

Although distinct Ni–O and Ag–O peaks were not observed in the FTIR spectra, XRD, EDX, and TEM analyses confirmed the presence of Ni and Ag in the Ni/MACB and Ag/Ni/MACB samples. This absence is expected, as Ni and Ag exist in their metallic nanoparticle forms (NiNPs and AgNPs), which do not exhibit strong infrared-active vibrations. Notably, a significant enhancement of the 1590 cm^{-1} peak in Ag/Ni/MACB compared
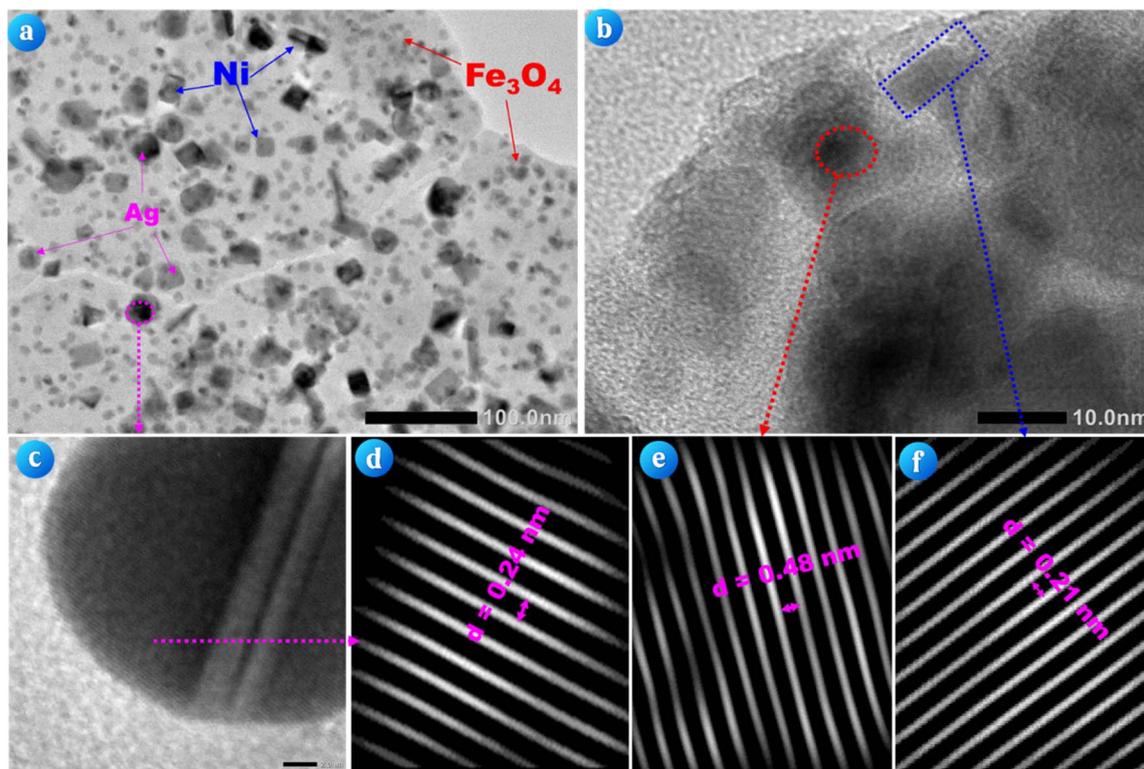
Fig. 3 (a) TEM image showing the surface morphology of the Ag/Ni/MACB composite; (b and c) magnified TEM images of selected nano-particles; (d–f) the lattice spacings (*d*-spacing) of Ag, Fe_3O_4, and Ni nanoparticles, respectively, obtained using ImageJ analysis.

to other samples suggests the influence of AgNPs. This enhancement may result from the surface-enhanced infrared absorption effect, where the localized surface plasmon resonance of AgNPs amplifies absorption signals, particularly for aromatic C=C bonds.[29] Additionally, AgNPs may interact with aromatic structures *via* π–metal interactions (Ag–π), increasing electron density and vibrational intensity. These findings highlight the role of AgNPs in modifying the surface chemistry and enhancing FTIR responses in the material.

3.1.4. Surface area and porosity analysis (BET). The surface area and porosity of the synthesized materials were evaluated using nitrogen adsorption–desorption isotherms and the BET method. The isotherms of all samples are provided in the ESI (Fig. S1),† while the nitrogen adsorption–desorption isotherm of the Ag/Ni/MACB sample is displayed in Fig. 4b. The textural properties, including BET surface area (S_{BET}), total pore volume, and pore diameter obtained from the Barrett–Joyner–Halenda (BJH) analysis, are summarized in Table 1. The BET surface areas of ACB, MACB, Ni/MACB, and Ag/Ni/MACB were determined to be 7.98, 2.51, 4.19, and 4.94 m^2 g^{-1}, respectively. A significant reduction in surface area was observed for all modified samples compared to ACB, likely due to structural modifications induced by the carbonization and activation process. The incorporation of Ni and Ag slightly mitigated this reduction, possibly by preventing excessive pore collapse during synthesis; however, the overall surface area remained lower than that of ACB.

The pore size distributions obtained from BJH analysis indicate that ACB exhibits a broader pore distribution (1–3 nm), suggesting the presence of both micropores and small mesopores. In contrast, MACB, Ni/MACB, and Ag/Ni/MACB predominantly feature pores in the 1–2 nm range, implying a shift toward smaller mesopores and enhanced microporosity after activation and metal incorporation (Fig. S1†). The nitrogen adsorption–desorption isotherms of the materials (Fig. 4b) exhibit a typical type IV profile with H3 hysteresis loops, characteristic of slit-shaped pores. The slight reduction in pore size after metal incorporation (Ni/MACB and Ag/Ni/MACB) might be due to partial pore blockage by the deposited metal species, though the mesoporous network remains largely intact. Overall, the surface area values obtained in this study are consistent with previously reported results for similar bead-based materials.[30,31] The relatively low BET surface areas are likely due to the spherical morphology of the samples, which can limit accessible surface area compared to powdered forms. However, the structural integrity and uniform dispersion of metal nanoparticles within the porous network may still facilitate catalytic applications where surface accessibility and active site availability are critical.

3.1.5. Optical properties analysis (PL and UV-Vis-DRS). Fig. 4c presents the PL spectra of ACB, MACB, Ni/MACB, and Ag/Ni/MACB, revealing emission peaks at approximately 387 nm, 464 nm, and a minor peak at 540 nm. The PL intensity of Ni/MACB and Ag/Ni/MACB is slightly higher than that of MACB
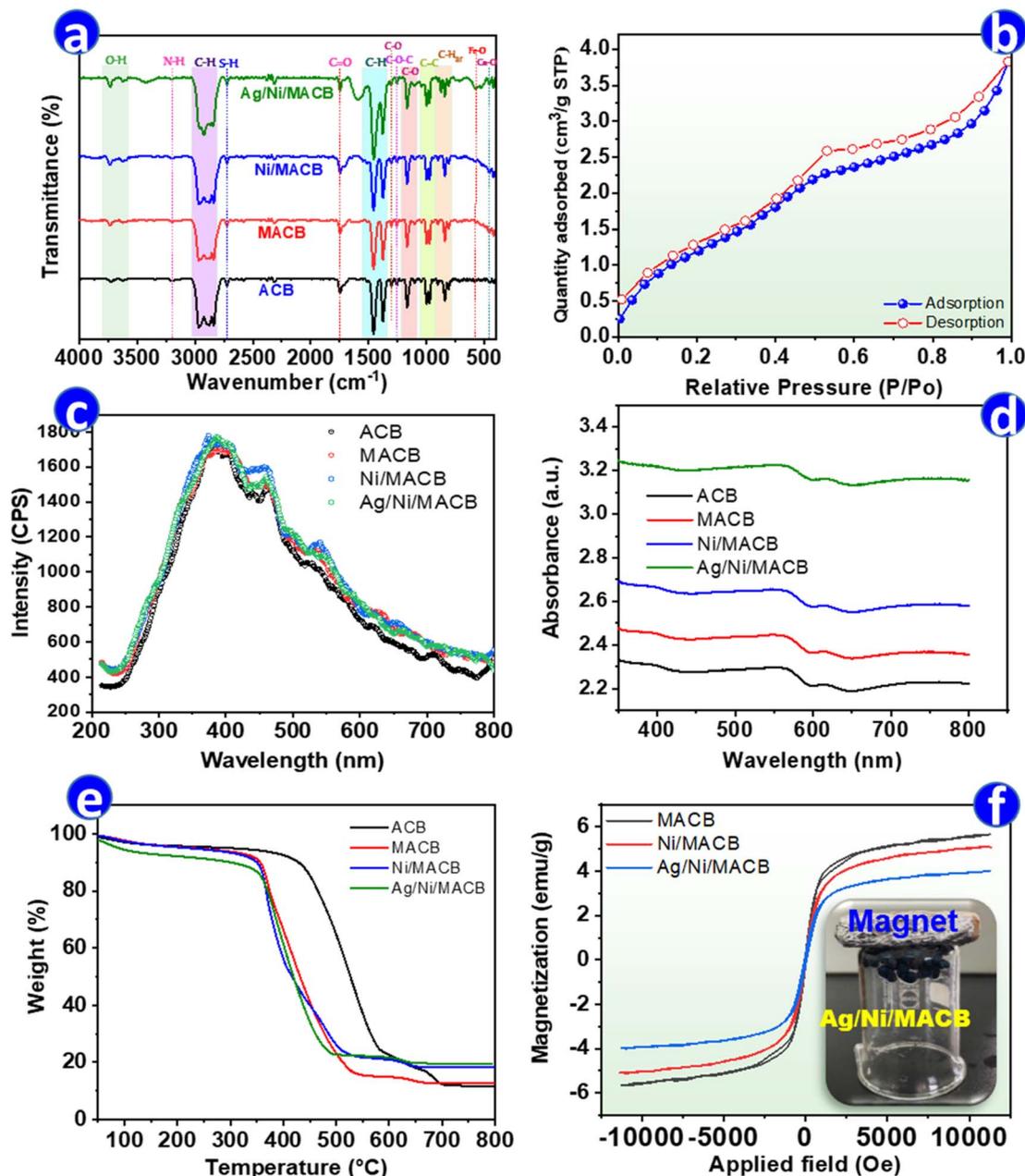
Fig. 4 Characterization of the synthesized samples: (a) FTIR spectra, (b) N_2 adsorption–desorption isotherm of Ag/Ni/MACB, (c) PL spectra, (d) UV-Vis DRS curves, (e) TGA profile, and (f) magnetization curves.

Table 1 Textural properties of the synthesized samples

Sample	S_{BET} ($m^2 g^{-1}$)	Pore volume[a] ($cm^3 g^{-1}$)	Pore diameter[a] (nm)
ACB	7.98	0.014	1.83
MACB	2.51	0.005	1.32
Ni/MACB	4.19	0.007	1.28
Ag/Ni/MACB	4.94	0.007	1.29

[a] Data from BJH analysis.

and ACB, which may initially suggest that the incorporation of Ni and Ag does not significantly suppress radiative electron–hole recombination. However, this increase in PL intensity could be attributed to the localized surface plasmon resonance effects of Ni and Ag nanoparticles, which can enhance photoluminescence emission rather than directly influencing charge separation.[32]

The UV-Vis DRS spectra (Fig. 4d) further confirm that the incorporation of Fe_3O_4, Ni, and Ag significantly enhances light absorption across the UV-visible range. The absorbance intensity follows the trend ACB < MACB < Ni/MACB < Ag/Ni/MACB, demonstrating the role of Ni and Ag in broadening the absorption range. The absence of a significant redshift in the absorption edge suggests that bandgap narrowing is not the primary factor. Instead, the enhanced photocatalytic performance of Ni/MACB and Ag/Ni/MACB likely arises from

a synergistic effect: improved light absorption, additional active catalytic sites, and facilitated interfacial charge transfer rather than bulk charge separation enhancement alone.[33] The presence of Fe_3O_4 provides Fenton-active sites, while Ni and Ag nanoparticles not only contribute to plasmonic effects but also enhance charge carrier utilization at the catalyst interface, thereby accelerating radical generation in the photo-Fenton process.

3.1.6. Thermal stability and magnetic properties (TGA and VSM). The thermal stability of ACB, MACB, Ni/MACB, and Ag/Ni/MACB was evaluated *via* TGA (Fig. 4e). All samples exhibited a multi-stage weight loss pattern, reflecting the decomposition of organic components and structural changes in the composite. The initial weight loss (below 360–400 °C) was relatively minor across all samples (~7–11%), attributed to the removal of adsorbed water and low-temperature decomposition of volatile organic matter. The primary decomposition stage occurred within 360–580 °C, corresponding to the degradation of the carbon matrix. Interestingly, metal-incorporated samples (MACB, Ni/MACB, Ag/Ni/MACB) exhibited earlier decomposition compared to pristine ACB, with major weight loss occurring in the ranges of 360–550 °C, 360–500 °C, and 360–490 °C, respectively. The earlier decomposition of metal-incorporated samples suggests that Fe_3O_4, Ni, and Ag acted as thermal adsorption sites, facilitating heat transfer and accelerating carbon degradation. Beyond 600 °C, further weight loss was minimal across all samples, indicating the formation of thermally stable residues. The total weight loss followed the order: ACB (86.92%) > MACB (86.49%) > Ni/MACB (81.03%) > Ag/Ni/MACB (78.95%), confirming that Ni and Ag doping improved thermal stability by reducing excessive carbon degradation.

The magnetic properties of MACB, Ni/MACB, and Ag/Ni/MACB were assessed using VSM (Fig. 4f). The saturation magnetization (M_s) values were 5.61, 5.08, and 3.96 emu g^{-1}, respectively, indicating a decrease in magnetization with increasing metal modification. While these M_s values are relatively low compared to bulk Fe_3O_4, they remain sufficient for efficient magnetic separation under an external magnetic field. The inset image in Fig. 4f visually demonstrates the magnetic response of Ag/Ni/MACB, where the material was successfully attracted and held in place by an external magnet, even when the vial was inverted. This confirms the practical applicability of Ag/Ni/MACB for facile recovery and reuse in catalytic applications.

3.2. Catalytic performance

The catalytic performance of Ag/Ni/MACB in different reaction systems for ENR removal was evaluated, and the results are presented in Fig. 5a. The comparison includes six different treatment conditions: H_2O_2 alone, H_2O_2 under light, adsorption by Ag/Ni/MACB (0.5) in the dark, photocatalysis with Ag/Ni/MACB under light, the Fenton process with Ag/Ni/MACB + H_2O_2 in the dark, and the photo-Fenton process with Ag/Ni/MACB + H_2O_2 under light. The experiment was conducted for 150 min without a pre-adsorption step, allowing direct evaluation of catalytic performance. As shown in Fig. 5a, H_2O_2 alone

exhibited minimal ENR removal (~15.28% after 150 min), indicating its weak oxidative capability without a catalyst. When H_2O_2 was exposed to light, the removal slightly increased to 18.47%, likely due to the photolysis of H_2O_2, generating a limited amount of hydroxyl radicals. In the adsorption test (Ag/Ni/MACB in the dark), the removal efficiency reached 21.61%, suggesting that the material has a moderate adsorption capacity for ENR. However, the removal through adsorption alone was still relatively low, indicating that catalytic processes play a crucial role in degradation. The Fenton process (Ag/Ni/MACB + H_2O_2 in the dark) significantly improved the removal efficiency to 29.59%. This enhancement can be attributed to the catalytic decomposition of H_2O_2 by active metal sites (Ni^{2+}/Fe^{3+}) on Ag/Ni/MACB, leading to the generation of reactive oxygen species (ROS) that facilitate ENR degradation.

A more substantial improvement was observed in the photocatalysis process with Ag/Ni/MACB under light, where the removal efficiency reached 54.37%. This result suggests that under light irradiation, Ag/Ni/MACB acts as an efficient photocatalyst, generating electron–hole pairs that promote oxidative degradation. The highest removal efficiency was achieved in the photo-Fenton process (Ag/Ni/MACB + H_2O_2 under light), reaching 62.33% after 150 min. This remarkable increase highlights the synergistic effect between the photocatalytic activity of Ag/Ni/MACB and the Fenton reaction, leading to an accelerated production of ROS under light irradiation. The combined mechanism enhances the oxidation and breakdown of ENR molecules, making the photo-Fenton process the most effective treatment method among the tested conditions.

A further evaluation was conducted by incorporating a 60 min pre-adsorption step before light irradiation (Fig. 5b). This modification led to an improved removal efficiency of 59.40% in the photocatalytic system and 96.78% in the photo-Fenton system, compared to 54.37% and 62.33%, respectively, without pre-adsorption (Fig. 5a). These results highlight the crucial role of adsorption in pollutant pre-concentration, allowing better interaction between ENR molecules and active catalytic sites. While the photocatalytic process alone demonstrated significant efficiency, the pre-adsorption step enhanced pollutant availability on the catalyst surface, leading to higher degradation. This phenomenon has been widely reported in previous studies, where the integration of adsorption with advanced oxidation processes, particularly the photo-Fenton reaction, has been shown to significantly enhance degradation efficiency by facilitating pollutant enrichment on the catalyst surface and increasing ROS-mediated oxidation.[34,35] This suggests that integrating a pre-adsorption phase can optimize catalytic performance, particularly in advanced oxidation processes, by maximizing pollutant–catalyst interactions.

To further compare the photo-Fenton efficiency of different materials, six catalysts—ACB, Ni/ACB, Fe_3O_4/ACB (MACB), Ag/ACB, Ni/MACB, and Ag/Ni/MACB—were evaluated under identical conditions, including a 60 min pre-adsorption step followed by 150 min of light irradiation (Fig. 5c). The final removal efficiencies were 38.36%, 42.39%, 46.81%, 50.77%, 62.97%, and 96.78%, respectively. The results indicate that ACB exhibited
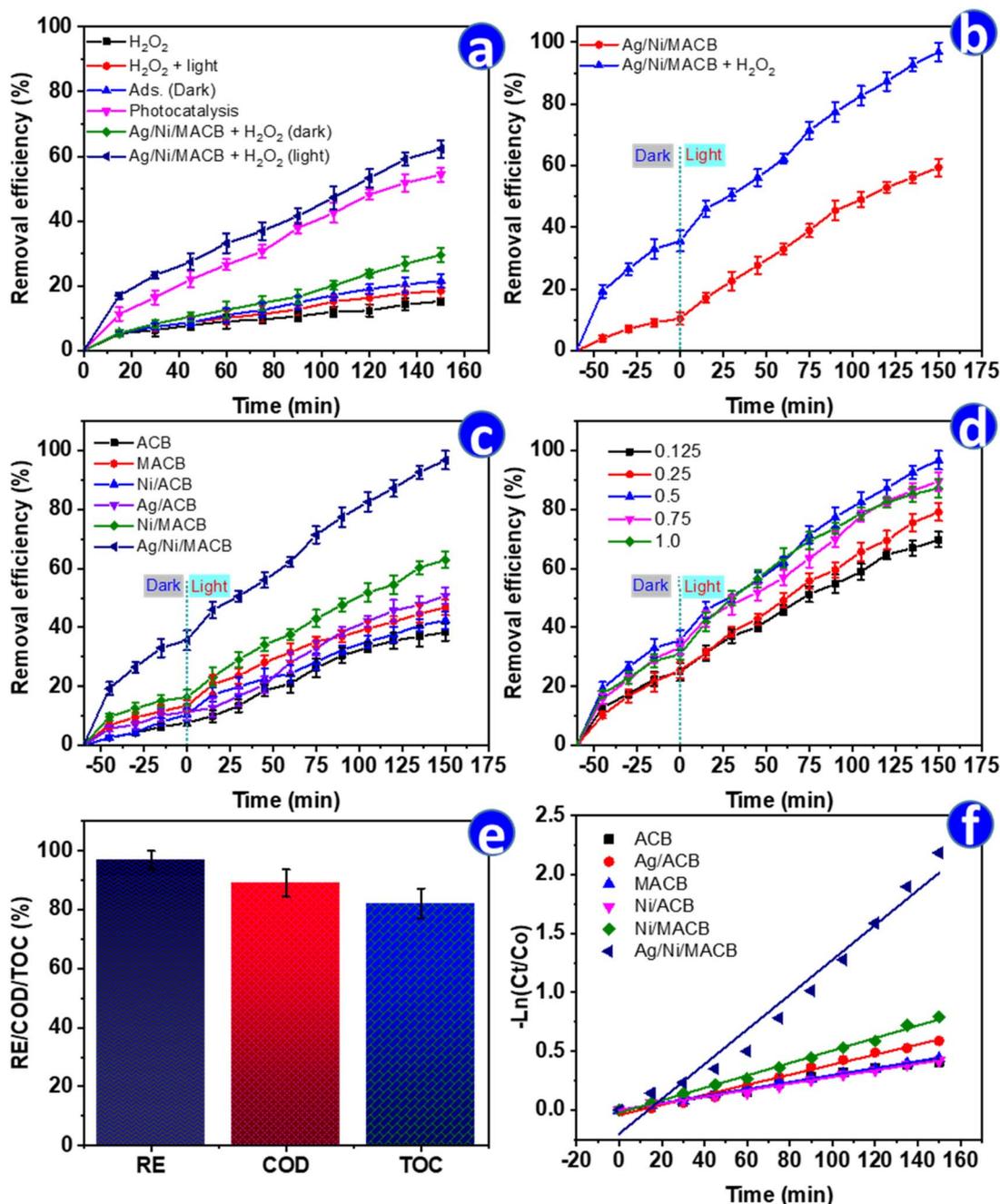
Fig. 5 Catalytic performance of Ag/Ni/MACB composites in ENR degradation under different conditions: (a) ENR removal in different systems (adsorption, photocatalysis, Fenton, and photo-Fenton); (b) ENR removal by Ag/Ni/MACB with and without H_2O_2 after 60 min dark adsorption; (c) comparison of different materials in ENR degradation; (d) influence of Ag content in Ag/Ni/MACB; (e) removal efficiency (RE), TOC, and COD reduction of Ag/Ni/MACB (0.5); (f) first-order kinetic plots of ENR degradation ($m = 8$ g L^{-1}, $C_{ENR} = 10$ mg L^{-1}, $C_{H_2O_2} = 0.05$ mol L^{-1}, pH = 7, $T = 25$ °C).

the lowest efficiency, emphasizing its limited intrinsic catalytic activity. The incorporation of Fe_3O_4 (MACB) significantly enhanced the removal efficiency (46.81%), surpassing that of Ni/ACB (42.39%). This suggests that Fe_3O_4 contributed more effectively to Fenton-like reactions than Ni, likely due to its superior ability to generate ROS *via* Fe^{2+}/Fe^{3+} cycling. The addition of Ni (Ni/MACB, 62.97%) further improved performance, reinforcing the role of Ni in H_2O_2 activation and

electron transfer. A particularly intriguing trend was observed in the case of Ag/ACB. During the initial 60 min of photo-Fenton reaction, its performance remained lower than MACB, Ni/ACB, and Ni/MACB, implying a slower activation process. However, after prolonged irradiation, its efficiency (50.77%) exceeded that of MACB. This suggests that Ag did not enhance Fenton-like activity as effectively as Fe_3O_4 but instead facilitated an alternative pathway. One plausible explanation is the plasmonic

effect of Ag nanoparticles under light irradiation, which enhances electron transfer and facilitates the reduction of ENR, potentially leading to structural modifications that contribute to its degradation.[36] This mechanism could explain the delayed but ultimately improved performance of Ag/ACB over Fe_3O_4-based MACB. The highest efficiency was achieved by Ag/Ni/MACB (96.78%), demonstrating the strong synergistic effect of Ag, Ni, and Fe_3O_4. In this system, Fe_3O_4 drove Fenton-like reactions, Ni facilitated H_2O_2 activation, and Ag provided additional catalytic reduction pathways, collectively maximizing pollutant degradation. These findings highlight the distinct but complementary roles of Fe_3O_4, Ni, and Ag in optimizing the photo-Fenton process, particularly the unexpected contribution of Ag in facilitating ENR reduction *via* plasmonic-driven catalysis.

To further elucidate the role of Ag in the enhanced performance of Ag/Ni/MACB, the effect of Ag content on ENR degradation was systematically investigated (Fig. 5d). The removal efficiency increased progressively from $0.125 \rightarrow 0.5$ Ag mol ratio, reaching a maximum of 96.78% at an Ag ratio of 0.5. However, further increasing the Ag ratio to 0.75 and 1.0 led to a slight decline in efficiency (89.57% and 87.16%, respectively). This trend suggests that the introduction of AgNPs initially improves degradation by enhancing electron transfer and promoting catalytic reduction *via* SPR. However, at excessive Ag loading, the aggregation of AgNPs likely reduces the available active sites and may interfere with Fe^{3+}/Fe^{2+} and Ni^{2+}/Ni cycling, thereby limiting the overall photo-Fenton efficiency. Interestingly, the performance of Ag/Ni/MACB (1.0) was comparable to that of Ag/Ni/MACB (0.5) during the first 75 min of reaction but exhibited a more pronounced decline beyond this point. This suggests that an excess of Ag may undergo oxidation or lead to competitive photon absorption, diminishing its long-term catalytic efficiency.

The catalytic performance of Ag/Ni/MACB was further evaluated in terms of COD and TOC removal (Fig. 5e). While ENR degradation reached 96.78%, COD and TOC removal efficiencies were 87.96% and 82.14%, respectively. The slightly lower COD removal efficiency compared to ENR degradation suggests that a fraction of the degraded ENR molecules persisted as partially oxidized intermediates rather than being fully mineralized. This observation aligns with the TOC removal results, indicating that complete mineralization into CO_2 and H_2O was not fully achieved.[37] The presence of residual organic byproducts is consistent with the multi-step degradation pathway in

photo-Fenton reactions, where hydroxyl radicals first cleave ENR into smaller organic fragments before subsequent oxidation to CO_2. These results confirm that Ag/Ni/MACB not only facilitates ENR degradation but also significantly reduces the overall organic pollutant load, demonstrating its practical potential for wastewater treatment applications.

To better understand the reaction kinetics, the degradation data were fitted to zero-order, first-order, and second-order models (Table 2 and Fig. 5f). While the correlation coefficients (R^2) varied among the models, the first-order kinetic model exhibited the best fit for Ag/Ni/MACB, with a high R^2 value of 0.9883. In contrast, the pseudo-second-order model showed a relatively poor fit ($R^2 = 0.822$), suggesting that the degradation process is better described by a first-order kinetic mechanism. The calculated rate constant ($k_1 = 0.0148$ min^{-1}) for Ag/Ni/MACB was approximately 5 times and 2.8 times higher than those of MACB and Ni/MACB, respectively, confirming the enhanced catalytic activity of the ternary composite. The catalytic performance of Ag/Ni/MACB was further assessed by comparing its efficiency with previously reported systems for ENR degradation (Table 3). As shown, Ag/Ni/MACB exhibited a high removal efficiency and a competitive reaction rate constant. These results highlight the strong catalytic activity of Ag/Ni/MACB, attributed to the synergistic effects of Fe_3O_4, Ni, and Ag in the photo-Fenton process.

3.3. Effects of reaction conditions

To optimize the degradation of ENR, the effects of key operational parameters—including pH, catalyst dosage, H_2O_2 concentration, initial ENR concentration, and temperature—were systematically evaluated (Fig. 6). pH plays a crucial role in the photo-Fenton process by influencing both catalyst surface charge and ENR speciation. As shown in Fig. 6a, the degradation efficiency followed a bell-shaped trend, increasing from 78.30% at pH 3 to a maximum of 96.78% at pH 7, before decreasing to 64.05% at pH 9. This trend is consistent with previous studies, such as Wei *et al.*, who observed a similar behavior when using KC_3N_4/Fh composite for photo-Fenton degradation of ENR.[2] The obtained results can be explained by the $pH_{pzc} = 6.4$ of Ag/Ni/MACB (Fig. 6b), where the catalyst surface is positively charged at pH < 6.4 and negatively charged at pH > 6.4. ENR, with $pK_{a_1} = 5.9$ and $pK_{a_2} = 8.0$, predominantly exists as a cation at pH < 5.9, a neutral species near pH 6–7, and an anion at pH > 8.[43] At acidic pH, the positively charged catalyst surface repels ENR cations, reducing adsorption and hindering

Table 2 Kinetic parameters for ENR degradation

Sample	Zero order		First order		Second order	
	k_0 (mg (L min)$^{-1}$)	R^2	k_1 (min^{-1})	R^2	k_2 (L (mg min)$^{-1}$)	R^2
ACB	0.0021	0.9748	0.0029	0.9859	0.0041	0.9853
MACB	0.0019	0.9890	0.003	0.9967	0.0048	0.9971
Ni/ACB	0.0019	0.9942	0.0028	0.9956	0.0042	0.9889
Ag/ACB	0.0027	0.9836	0.0043	0.9881	0.0068	0.9831
Ni/MACB	0.0028	0.9955	0.0053	0.9948	0.0103	0.9695
Ag/Ni/MACB	0.0036	0.9858	0.0148	0.9883	0.0799	0.822

Table 3 Comparison of ENR removal efficiency and reaction rate constants using different catalytic systems

Catalyst	Reaction type	Conditions	k (min^{-1})/RE (%)	Ref.
Fe–N–C@ZnO	Photocatalytic	[ENR] = 10 mg L^{-1}, [catalyst] = 1 g L^{-1}, pH 7, 120 min of vis. irradiation	0.023/95.0	37
GaOOH/ZnBiTaO$_5$	Photocatalytic	[ENR] = 10 mg L^{-1}, [catalyst] = 1 g L^{-1}, 60 min of solar light irradiation	0.0143/58.3	38
Bi$_{12}$O$_{17}$Cl$_2$/Ag$_2$CrO$_4$	Photocatalytic	[ENR] = 20 mg L^{-1}, [catalyst] = 0.5 g L^{-1}, 60 min of LED light irradiation	0.0303/85.5	39
n-MnOx	Oxidation	[ENR] = 10 mg L^{-1}, n-MnOx 5 g L^{-1}, pH 4	0.067/88.0	40
Ag$_2$O/CeO$_2$	Photocatalytic	[ENR] = 10 mg L^{-1}, [catalyst] = 1 g L^{-1}, pH 7, 120 min of vis. irradiation	0.0147/87.1	41
SnZVI@PPC-2	Bio-electro-Fenton	[ENR] = 10 mg L^{-1}, pH = 7.4, 72 h	—/86.2	42
Ag/Ni/MACB	Photo-Fenton	[ENR] = 10 mg L^{-1}, [catalyst] = 8 g L^{-1}, pH 7, 150 min of vis. irradiation	0.0148/96.78	This study

degradation efficiency. At neutral pH, repulsion between the catalyst and ENR is minimized, facilitating better adsorption and degradation. In contrast, at pH > 8, both the catalyst surface and ENR molecules become negatively charged, leading to electrostatic repulsion that further reduces degradation efficiency. Additionally, excessive OH$^-$ ions at high pH may promote the formation of Fe(OH)$_3$ and Ni(OH)$_2$ precipitates, reducing the availability of Fe^{2+} and Ni^{2+} as active species for the Fenton and photo-Fenton reactions, thereby limiting the catalytic efficiency.

The effect of catalyst dosage is illustrated in Fig. 6c. Increasing the catalyst dosage from 4 to 8 g L^{-1} enhanced degradation efficiency from 88.08% to 96.78%, as more active sites were available. However, at 10 g L^{-1}, the efficiency dropped slightly to 90.95%, despite exhibiting the highest removal rate during the first 100 min. This decline in the final stage may be attributed to the light shielding effect at high catalyst concentrations, reducing photon penetration and radical generation. Additionally, excessive catalyst dosage might accelerate the decomposition of H$_2$O$_2$ into O$_2$ rather than ˙OH, or promote radical recombination, ultimately limiting degradation efficiency.[44]

The role of H$_2$O$_2$ concentration was also examined (Fig. 6d). The efficiency increased with increasing H$_2$O$_2$ concentration, reaching a maximum of 96.78% at 0.05 M, before slightly decreasing at 0.075 M (91.86%) and 0.1 M (90.59%). This trend indicates that while H$_2$O$_2$ acts as a source of ˙OH radicals, excessive amounts can lead to radical scavenging via eqn (10), resulting in the formation of less reactive HO$_2^˙$ radicals and reducing degradation efficiency.[45] Notably, the observed trends in the effects of catalyst dosage and H$_2$O$_2$ concentration in this study align with the findings of Amari et al., who reported a similar pattern when employing Fe$_2$O$_3$/Bi$_2$O$_3$/In$_2$S$_3$ for the visible-light-driven degradation of ENR.[3] This resemblance suggests that both systems share comparable reaction dynamics, where an optimal balance between active sites and reactive species is crucial for maximizing degradation efficiency.

$$H_2O_2 + {^˙OH} \rightarrow HO_2^˙ + H_2O \qquad (10)$$

The initial ENR concentration significantly affected degradation efficiency (Fig. 6e). While removal remained high at 5 mg L^{-1} (91.23%) and 10 mg L^{-1} (96.78%), it decreased at 15 mg L^{-1} (87.89%) and 20 mg L^{-1} (79.80%). This behavior is likely due to radical-to-pollutant ratio limitations, where higher ENR concentrations consume available ˙OH radicals faster, leaving insufficient oxidants for complete degradation.[42] Finally, temperature had a notable impact on degradation efficiency (Fig. 6f). The efficiency decreased from 96.78% at 25 °C to 59.20% at 55 °C, indicating that higher temperatures may accelerate H$_2$O$_2$ decomposition into oxygen, reducing ˙OH availability, or promote side reactions that inhibit radical formation. This trend deviates from typical thermally activated processes, highlighting the temperature-sensitive nature of the Ag/Ni/MACB-based photo-Fenton reaction. These findings indicate that the optimal conditions for ENR degradation using Ag/Ni/MACB are room temperature (25 °C), a catalyst dosage of 8 g L^{-1}, an initial ENR concentration of approximately 10 mg L^{-1}, an H$_2$O$_2$ concentration of 0.05 mol L^{-1}, and a neutral pH of 7.

Inorganic ions are typically present in real wastewater and can significantly influence the performance of advanced oxidation processes. To evaluate the effect of commonly encountered ions on the degradation of ENR, several representative inorganic species—including HCO$_3^-$, H$_2$PO$_4^-$, Cl$^-$, NO$_3^-$, SO$_4^{2-}$, Ca^{2+}, and Mg^{2+} (at a concentration of 1 mM)—were individually introduced into the reaction system under optimized conditions. As shown in Fig. S2,† the degradation efficiency in the absence of any added ions was 96.78%. The presence of most ions led to a slight decline in removal efficiency. Notably, bicarbonate (HCO$_3^-$) and phosphate (H$_2$PO$_4^-$) exhibited the strongest inhibitory effects, reducing the efficiency to 81.23% and 85.91%, respectively. This can be attributed to their radical scavenging properties, especially toward hydroxyl radicals, which are key reactive species in the photo-Fenton system. In contrast, SO$_4^{2-}$ and NO$_3^-$ had minimal effects, maintaining relatively high removal rates of 94.28% and 92.15%, likely due to their weaker interaction with ROS. Monovalent Cl$^-$ and divalent cations such as Ca^{2+} and Mg^{2+} caused moderate suppression (87.55–90.64%), possibly due to
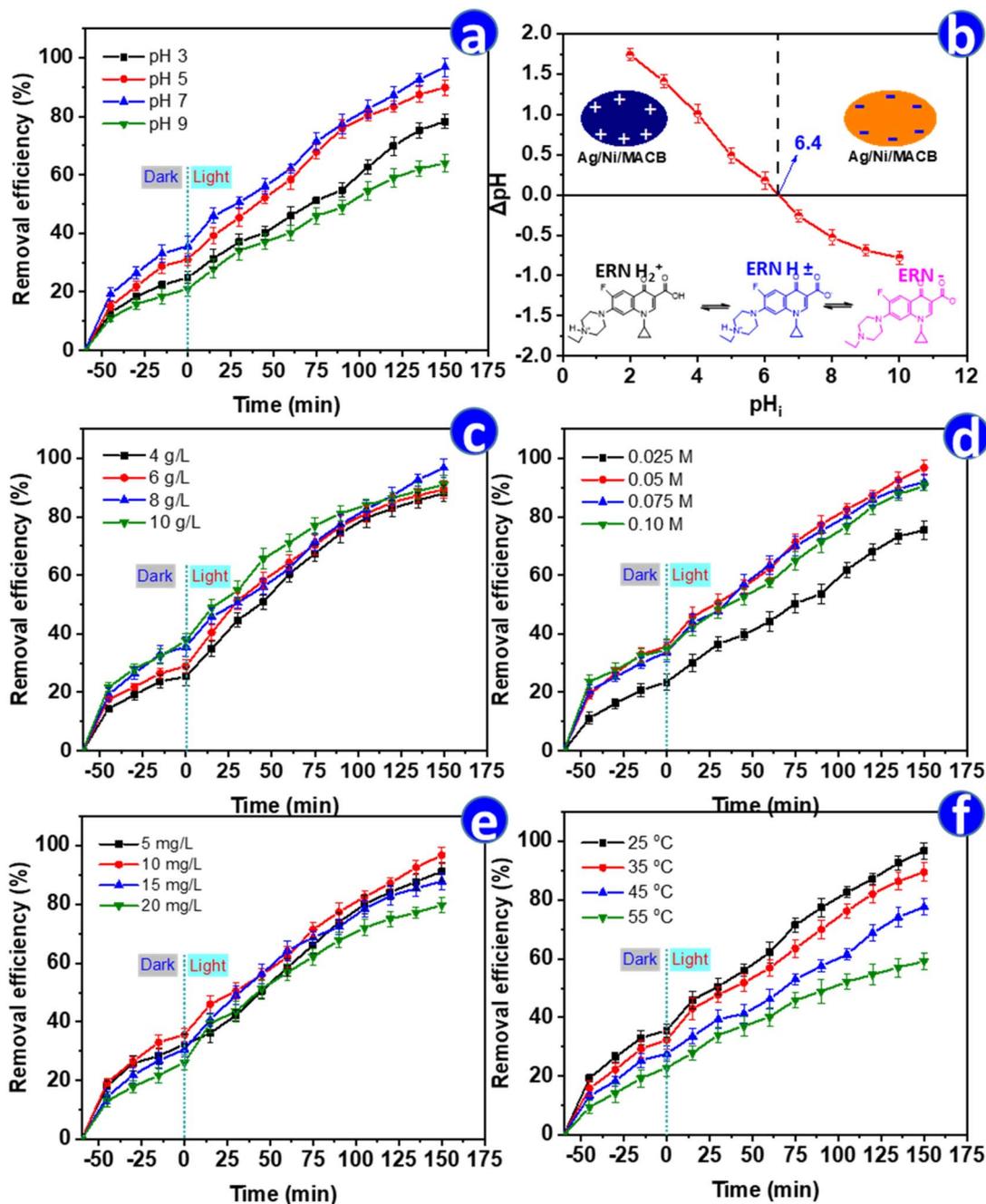
Fig. 6 Effect of reaction parameters on the degradation of ENR using Ag/Ni/MACB: (a) effect of pH, (b) plot of ΔpH *versus* initial pH for determining pH_{pzc}, along with the surface charge of Ag/Ni/MACB and ERN as a function of pH, (c) effect of catalyst dosage, (d) effect of H_2O_2 concentration, (e) effect of initial enrofloxacin concentration, and (f) effect of temperature.

surface competition or changes in surface charge dynamics.[46] These findings indicate that while the Ag/Ni/MACB system remains robust in the presence of common ions, strong radical scavengers like bicarbonate and phosphate could negatively affect its performance in practical wastewater matrices.

3.4. Possible degradation mechanism

To elucidate the degradation mechanism of ENR in the presence of Ag/Ni/MACB under photo-Fenton conditions, radical scavenging experiments were conducted to determine the dominant ROS involved in the degradation process. As presented in Fig. 7a, the degradation efficiency of ENR reached 96.78% in the absence of scavengers. However, when different scavengers were introduced, a significant decline in degradation efficiency was observed, indicating the involvement of multiple ROS in the reaction pathway. In particular, the addition of IPA, a ·OH scavenger, dramatically reduced the degradation efficiency to 31.32%, suggesting that ·OH played a major

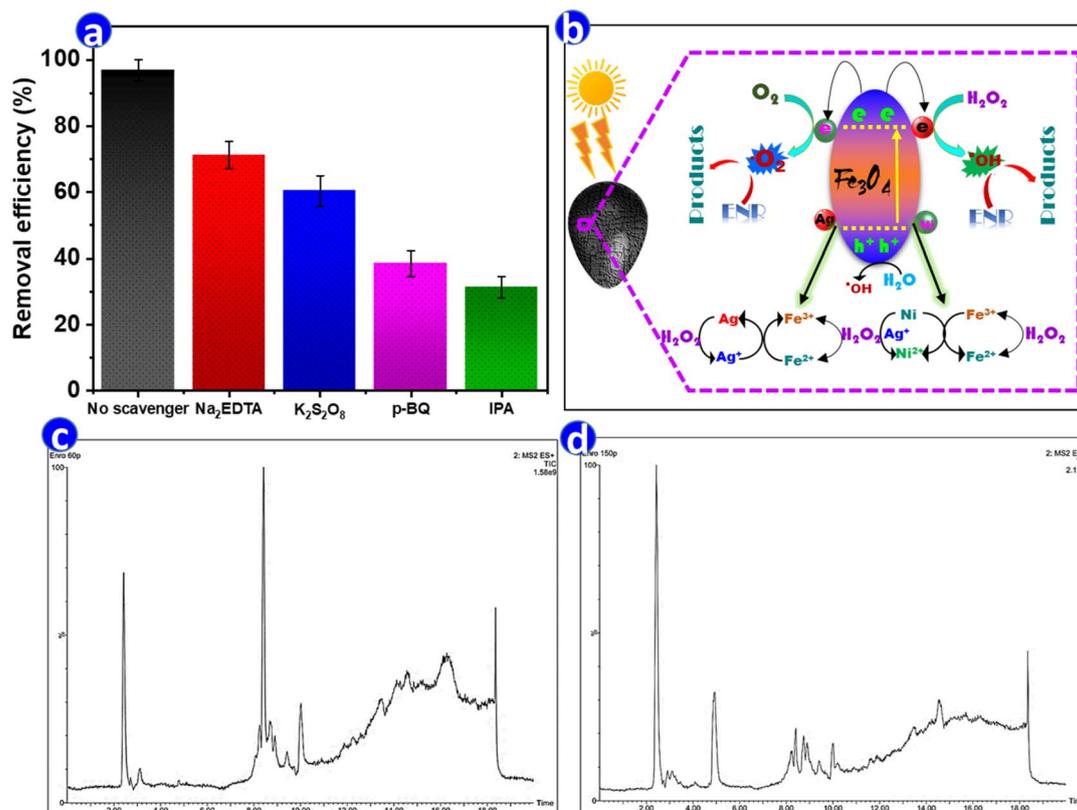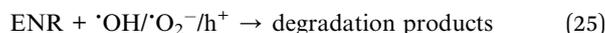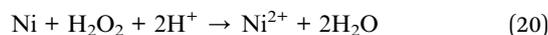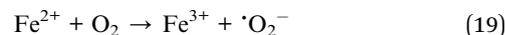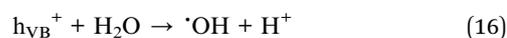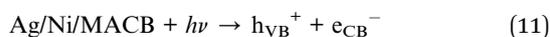Fig. 7 (a) Degradation performance of ENR in the presence of different scavengers; (b) proposed degradation mechanism; (c and d) total ion chromatograms (TIC) of the ENR solution after photo-Fenton catalytic degradation by Ag/Ni/ACB at 60 min (c) and 150 min (d).

role in ENR degradation. Similarly, the presence of *p*-BQ, a scavenger for superoxide radicals ($O_2^{\bullet-}$), led to a decrease in degradation efficiency to 38.36%, indicating that $O_2^{\bullet-}$ also contributed to the degradation process. The introduction of Na_2EDTA, a well-known hole (h^+) scavenger, resulted in a degradation efficiency of 71.2%, suggesting that photo-generated holes participated in the oxidation of ENR. Moreover, the addition of $K_2S_2O_8$, an electron acceptor that suppresses electron transfer, further lowered the degradation efficiency to 60.38%, supporting the role of electron transfer in ROS generation. Based on these findings, a possible degradation mechanism is proposed, as illustrated in Fig. 7b and described by eqn (11)–(25).

$$Ag/Ni/MACB + h\nu \rightarrow h_{VB}^+ + e_{CB}^- \qquad (11)$$

$$e_{CB}^- \rightarrow e_M^- \ (M = Ni, Ag) \qquad (12)$$

$$H_2O_2 + h\nu \rightarrow 2\,^{\bullet}OH \qquad (13)$$

$$e_M^- + H_2O_2 \rightarrow \,^{\bullet}OH + OH^- \qquad (14)$$

$$e_M^- + O_2 \rightarrow \,^{\bullet}O_2^- \qquad (15)$$

$$h_{VB}^+ + H_2O \rightarrow \,^{\bullet}OH + H^+ \qquad (16)$$

$$Fe^{3+} + H_2O_2 \rightarrow Fe^{2+} + HO_2^{\bullet} + H^+ \qquad (17)$$

$$Fe^{2+} + H_2O_2 \rightarrow Fe^{3+} + \,^{\bullet}OH + OH^- \qquad (18)$$

$$Fe^{2+} + O_2 \rightarrow Fe^{3+} + \,^{\bullet}O_2^- \qquad (19)$$

$$Ni + H_2O_2 + 2H^+ \rightarrow Ni^{2+} + 2H_2O \qquad (20)$$

$$Ni + 2Fe^{3+} \rightarrow Ni^{2+} + 2Fe^{2+} \qquad (21)$$

$$Ag + 2H_2O_2 \rightarrow Ag^+ + \,^{\bullet}O_2^- + 2H_2O \qquad (22)$$

$$Ag^+ + Fe^{2+} \rightarrow Fe^{3+} + Ag \qquad (23)$$

$$Ni + 2Ag^+ \rightarrow Ni^{2+} + 2Ag \qquad (24)$$

$$ENR + \,^{\bullet}OH/^{\bullet}O_2^-/h^+ \rightarrow degradation\ products \qquad (25)$$

Upon irradiation, Fe_3O_4 within the Ag/Ni/MACB composite absorbs photon energy, exciting electrons from the valence band to the conduction band (eqn (11)). The photogenerated electrons (e_{CB}^-) migrate to the metal nanoparticles (Ni, Ag), facilitating charge separation and preventing electron–hole recombination (eqn (12)). Meanwhile, H_2O_2 undergoes photolysis to generate hydroxyl radicals (eqn (13)). The transferred electrons participate in redox reactions, where they reduce H_2O_2 to generate $^{\bullet}OH$ and hydroxide ions (eqn (14)) and react with molecular oxygen (O_2) to form superoxide radicals (eqn (15)).

The photogenerated holes in Fe_3O_4 also contribute to $^\bullet OH$ formation through water oxidation (eqn (16)). Additionally, Fe^{3+}/Fe^{2+} cycles play a crucial role in the Fenton-like reactions, where Fe^{3+} is reduced by H_2O_2 to Fe^{2+}, producing hydroperoxyl radicals ($HO_2^\bullet$) (eqn (17)), while Fe^{2+} further reacts with H_2O_2 to generate $^\bullet OH$ (eqn (18)). Fe^{2+} also interacts with O_2 to regenerate Fe^{3+} and form $^\bullet O_2^-$ (eqn (19)), sustaining ROS production. Ni and Ag nanoparticles further enhance the catalytic process. Ni reacts with H_2O_2, contributing to additional Ni^{2+} formation (eqn (20)), while electron transfer between Ni and Fe_3O_4 facilitates Fe^{2+} regeneration (eqn (21)). Ag nanoparticles participate in H_2O_2 decomposition, generating $^\bullet O_2^-$ species (eqn (22)), and Ag^+ ions undergo redox cycling with Fe^{2+} (eqn (23)) and Ni (eqn (24)), further amplifying the catalytic effect. Ultimately, the generated ROS, including $^\bullet OH$, $^\bullet O_2^-$, and photogenerated holes, attack ENR molecules, leading to their degradation into smaller intermediates and final mineralization (eqn (25)).[47,48]

To elucidate the degradation mechanism of enrofloxacin (ENR) under the Ag/Ni/MACB-catalyzed photo-Fenton process, the total ion chromatograms (TIC) of ENR solutions at different reaction times were analyzed (Fig. 7c and d). The TIC spectra at 60 min (Fig. 7c) and 150 min (Fig. 7d) reveal notable changes in peak intensities and the emergence/disappearance of several peaks, indicating the progressive degradation of ENR. Compared to the TIC profile at 60 min, the peak at RT = 2.451 min exhibited an increase in intensity, with mass spectrometry (MS) analysis (see Fig. S3 and S4†) revealing a dominant fragment at $m/z = 85$, suggesting the accumulation of small degradation fragments over time. The peak at RT = 3.129 min disappeared, with its MS spectrum showing fragments at $m/z = 99$ and 118, implying that these intermediates underwent further transformation. A new peak emerged at RT = 4.937 min, with a primary ion at $m/z = 143$, indicating the formation of a newly generated intermediate. The peak at RT =

8.414 min significantly decreased in intensity, with MS analysis showing a major fragment at $m/z = 360$, which corresponds to ENR, confirming its continuous degradation. The peak at RT = 9.996 min also decreased, with its MS spectrum revealing a predominant ion at $m/z = 274$, suggesting that the intermediate products continued to degrade.

Based on these observations, the identified mass fragments, and previously published studies,[49] a possible degradation pathway for ENR was proposed (Fig. 8). The initial attack on ENR likely involved cleavage mediated by hydroxyl radicals and superoxide radicals, leading to successive fragmentation and the formation of smaller intermediates. The continuous decrease in ENR intensity and the accumulation of small fragments over time further corroborate the effective catalytic degradation of ENR under the photo-Fenton system.

3.5. Stability and reusability study

The stability and reusability of Ag/Ni/MACB were evaluated through five consecutive photo-Fenton cycles, with the results presented in Fig. 9a. The removal efficiency of ENR gradually decreased from 96.78% in the first cycle to 83.61% after the fifth cycle, suggesting a slight decline in catalytic performance over multiple reuses. This reduction may be attributed to the partial deactivation of active sites due to surface fouling by reaction intermediates or minor structural modifications of the catalyst. To further investigate the structural integrity of Ag/Ni/MACB after repeated use, SEM, XRD, and FTIR analyses were performed (Fig. 9b–d). The SEM image (Fig. 9b) reveals that metal nanoparticles still uniformly dispersed on the ACB surface, indicating good morphological stability. XRD analysis (Fig. 9c) further confirms that the primary crystalline phases remained intact after multiple cycles, with no significant phase transformation observed. Similarly, the FTIR spectra (Fig. 9d) before
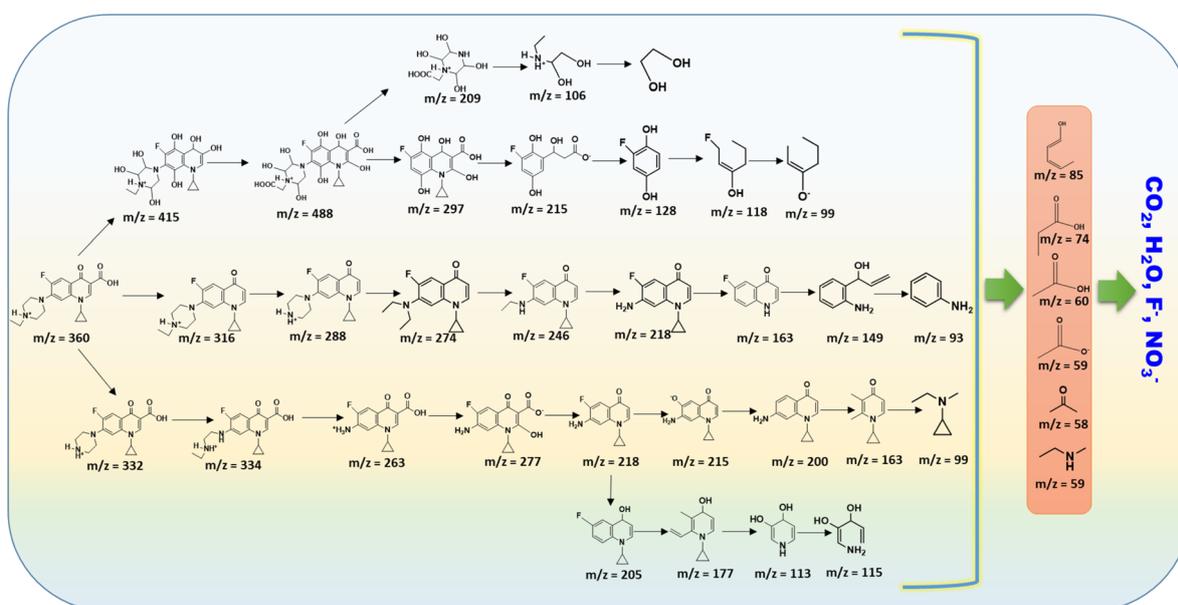

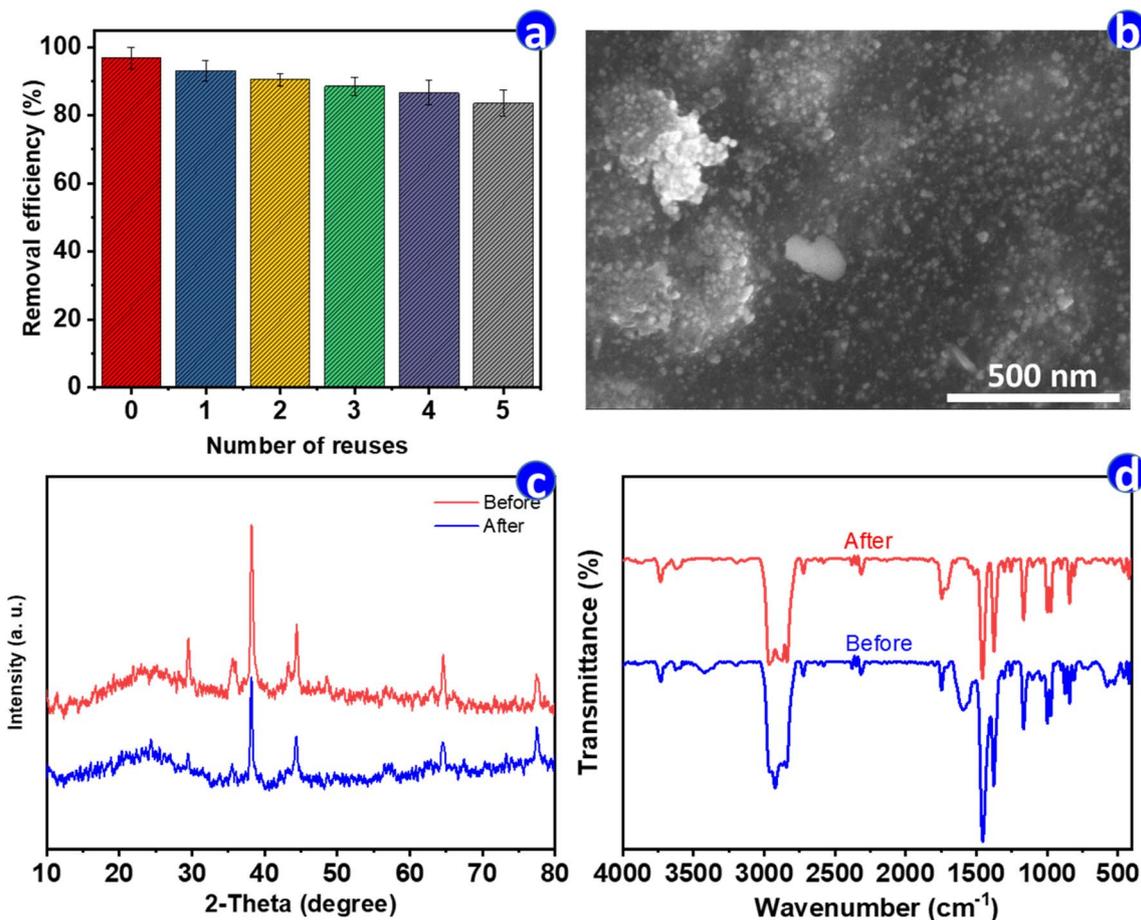**Fig. 8** Proposed pathway for the degradation of ENR by Ag/Ni/MACB.

Fig. 9 Stability and reusability of Ag/Ni/MACB: (a) removal efficiency of ENR over multiple recycling cycles; (b) SEM image, (c) XRD pattern, and (d) FTIR spectrum of the catalyst after multiple reuse cycles.

and after use exhibit only minor shifts in peak positions and a slight decrease in intensity, suggesting that the catalyst's functional groups were largely preserved. However, the minor spectral changes could be associated with the adsorption of residual intermediates on the catalyst surface. Leaching of Fe, Ni, and Ag into solution was analyzed using ICP-MS to assess catalyst stability. The measured concentrations of Fe, Ni, and Ag in the first cycle were 120.7, 52.8, and 14.1 ppb, respectively,
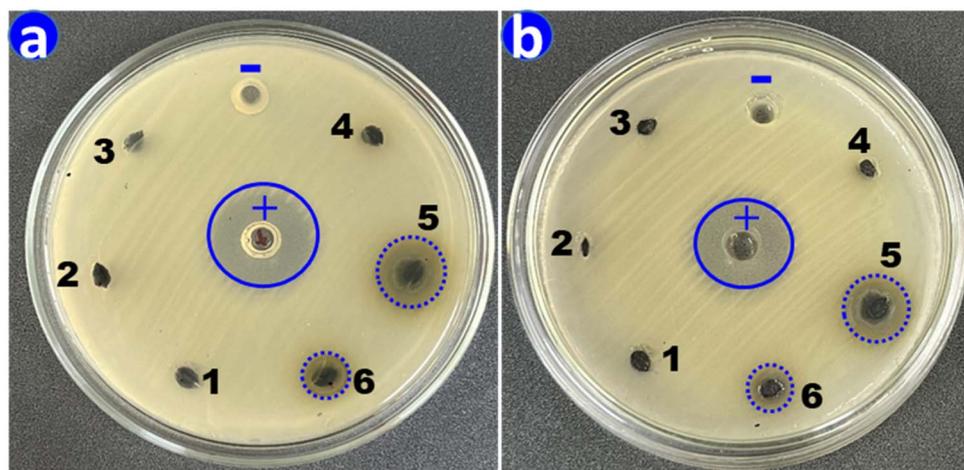

Fig. 10 Antibacterial activity of synthesized samples against *E. coli* (a) and *S. aureus* (b). (+): gentamicin antibiotic, (−): sterile distilled water, (1) ACB, (2) MACB, (3) Ni/ACB, (4) Ni/MACB, (5) Ag/ACB, and (6) Ag/Ni/MACB.

while these values decreased to 100.6, 27.3, and 4.5 mg L^{-1} in the fifth cycle. Importantly, all leached metal concentrations remained well below the maximum permissible limits set by the Vietnamese National Technical Regulation on Drinking Water Quality (QCVN 01-1:2018/BYT), indicating that Ag/Ni/MACB exhibits excellent structural stability with minimal metal leaching, making it a promising and environmentally safe catalyst for wastewater treatment applications.

3.6. Antibacterial ability

The antibacterial activity of the synthesized materials was evaluated against *E. coli* and *S. aureus* using an agar diffusion test, in which intact catalyst beads were directly placed onto the agar surface (Fig. 10). The results showed that ACB, MACB, Ni/ACB, and Ni/MACB exhibited no observable inhibition zones against either bacterial strain, indicating that Fe$_3$O$_4$ and Ni did not contribute to antibacterial activity. In contrast, the Ag-containing samples (Ag/ACB and Ag/Ni/MACB) demonstrated significant antibacterial effects, confirming the key role of silver in bacterial inhibition. For the positive control, gentamicin exhibited inhibition zone diameters of 2.10 ± 0.10 cm and 1.90 ± 0.10 cm against *E. coli* and *S. aureus*, respectively. The Ag/ACB sample exhibited inhibition zones of 1.7 cm and 1.5 cm, while Ag/Ni/MACB showed slightly lower inhibition diameters of 1.10 ± 0.10 cm and 0.90 ± 0.05 cm against *E. coli* and *S. aureus*, respectively. The reduced antibacterial activity of Ag/Ni/MACB compared to Ag/ACB can be attributed to its lower silver content, resulting in decreased silver ion release. These findings confirm that Ag incorporation imparts antibacterial properties to the catalyst, making it a potential multifunctional material for environmental applications.

4. Conclusions

This study successfully developed a one-pot green-synthesized Ag/Ni/Fe$_3$O$_4$-activated carbon bead (Ag/Ni/MACB) catalyst using *Brucea javanica* as a natural carbon precursor. The millimeter-sized porous beads exhibited excellent photo-Fenton activity, ease of recovery, and antibacterial functionality, making them a promising alternative to conventional powdered catalysts. Under optimized conditions (pH = 7, catalyst dosage = 8 g L^{-1}, H$_2$O$_2$ concentration = 0.05 M, initial ENR concentration = 10 mg L^{-1}), Ag/Ni/MACB achieved 96.78% enrofloxacin (ENR) removal within 150 min under visible-light irradiation. Mechanistic studies revealed that hydroxyl radicals and superoxide radicals were the dominant reactive species driving ENR degradation, and the reaction pathway was elucidated through LC-MS/MS analysis. The catalyst also exhibited strong antibacterial activity against *Escherichia coli* and *Staphylococcus aureus*, demonstrating its dual-functionality in wastewater treatment. Furthermore, Ag/Ni/MACB retained 83.61% efficiency after five cycles, with negligible metal leaching, confirming its stability and reusability. Despite these advantages, some limitations remain. The catalyst showed a gradual decrease in efficiency over repeated cycles, suggesting potential surface fouling or minor structural degradation.

Additionally, the underlying interaction mechanisms between Ag, Ni, and Fe$_3$O$_4$ in the composite require further investigation to optimize catalytic performance. Future work should focus on enhancing long-term stability, minimizing catalyst deactivation, and scaling up production for real-world wastewater treatment applications. Moreover, studying the toxicity and environmental impact of Ag leaching over prolonged use is crucial to ensure safety in practical applications. Overall, this study highlights the potential of Ag/Ni/MACB as a multifunctional and sustainable catalyst for simultaneous antibiotic degradation and microbial disinfection, paving the way for advanced materials in next-generation wastewater treatment technologies.

Data availability

All data generated or analyzed during this study are included in this published article.

Conflicts of interest

There are no conflicts to declare.

Acknowledgements

References

1 J. Pan, H. Sun, K. Chen, Y. Zhang, P. Shan, W. Shi and F. Guo, *Chin. J. Chem. Eng.*, 2023, **54**, 162–172.
2 S. Wei, L. Zhang, Z. Guo and D. Dong, *Chem. Eng. J.*, 2024, **500**, 157403.
3 A. Amari, A. B. M. Ali, M. A. Ismail, M. A. Diab, H. A. El-Sabban, E. Saitov, A. Reyimberganov and N. Elboughdiri, *Surf. Interfaces*, 2025, **58**, 105816.
4 T. D. Nguyen, X. M. Vu, T. F. Kouznetsova, T. L. Pham, L. A. Kapysh, A. I. Ivanets, T. M. H. Le, V. C. Bui, H. T. Nguyen and V. D. Doan, *J. Porous Mater.*, 2025, DOI: 10.1007/s10934-024-01741-2.
5 W. Shi, W. Sun, Y. Liu, K. Zhang, H. Sun, X. Lin, Y. Hong and F. Guo, *J. Hazard. Mater.*, 2022, **436**, 129141.
6 F. Machado, A. C. S. C. Teixeira and L. A. M. Ruotolo, *Int. J. Environ. Sci. Technol.*, 2023, **20**, 13995–14032.
7 Q. Wang, R. Zhao, H. Li, S. Sun, Y. Sun, W. Gu, N. Wang and X. Li, *Sep. Purif. Technol.*, 2025, **359**, 130546.
8 V. T. Le, V. D. Doan, V. A. Tran, H. S. Le, D. L. Tran, T. M. Pham, T. H. Tran and H. T. Nguyen, *Mater. Res. Bull.*, 2020, **129**, 110913.
9 T. T. N. Le, H. B. Truong, L. Thi Hoa, H. S. Le, T. T. T. Tran, T. D. Manh, V. T. Le, Q. K. Dinh and X. C. Nguyen, *Heliyon*, 2023, **9**, e20466.

10 O. Tammaro, N. Morante, A. Marocco, M. Fontana, M. Castellino, G. Barrera, P. Allia, P. Tiberto, R. Arletti, R. Fantini, V. Vaiano, S. Esposito, D. Sannino and M. Pansini, *Chemosphere*, 2023, **345**, 140400.

11 B. Bai, G. Cheng, J. Chen, X. Chen and Q. Wang, *Catalysts*, 2024, **14**, 453.

12 A. Zhang, L. Zhu and Z. Nan, *Mater. Chem. Phys.*, 2019, **224**, 156–168.

13 K. Sundaresan, S. Mohan, K. Tharini, N. Arumugam, A. I. Almansour and K. Perumal, *Biomass Convers. Biorefin.*, 2025, **15**, 4539–4550.

14 C. Wu, T. Guo, Y. Chen, Q. Tian, Y. Zhang, Z. Huang, H. Hu and T. Gan, *Sep. Purif. Technol.*, 2024, **329**, 125174.

15 O. Amiri, F. Beshkar, S. S. Ahmed, B. W. Hamad, P. H. Mahmood and A. A. Dezaye, *Int. J. Hydrogen Energy*, 2021, **46**, 19913–19925.

16 F. S. Safavi, S. Y. Ebrahimipour, S. J. Fatemi, P. Mohammadi and T. Shamspur, *Biomass Convers. Biorefin.*, 2025, DOI: **10.1007/s13399-025-06541-5**.

17 J. Zhang, H.-X. Xu, Y.-X. Dou, Q.-H. Huang, Y.-F. Xian and Z.-X. Lin, *Front. Pharmacol.*, 2022, **13**, 853119.

18 V. T. Le, T. K. N. Tran, D. L. Tran, H. S. Le, V. D. Doan, Q. D. Bui and H. T. Nguyen, *J. Dispersion Sci. Technol.*, 2019, **40**, 1761–1776.

19 S.-C. Shen, S.-L. Xu, S. Zhao, L.-L. Zhang, S.-Q. Chu and H.-W. Liang, *ACS Sustain. Chem. Eng.*, 2022, **10**, 731–737.

20 T. Pan, J. Jiang, Y. Li, T. Zhong, H. Wang, C. Pu and P. Jin, *Int. J. Electrochem. Sci.*, 2024, **19**, 100554.

21 Q. U. Ain, U. Rasheed, Z. Chen, R. He and Z. Tong, *J. Ind. Eng. Chem.*, 2024, **134**, 327–342.

22 H. Chen, P. Hao, J. Liu, G. Zhou, X. Lv, R. Zhang, Y. Wei, W. Li, S. Zhou and X. Feng, *Appl. Surf. Sci.*, 2025, **692**, 162756.

23 H. T. Nguyen, M. T. Truong, V.-D. Doan, T. L. H. Nguyen, V. H. Hoang, V. A. Tran, A.-T. Nguyen and V. T. Le, *Chem. Eng. Sci.*, 2024, **284**, 119487.

24 D. Yang, Y. Lei, Z. Fan, W. Chen and F. Wan, *Microchem. J.*, 2024, **207**, 112295.

25 O. Ola, H. Ullah, Y. Chen, K. Thummavichai, N. Wang and Y. Zhu, *J. Mater. Chem. C*, 2021, **9**, 6409–6417.

26 I. Fatimah, G. D. Ramanda, S. Sagadevan, Suratno, M. Tamyiz and R. Doong, *Case Stud. Chem. Environ. Eng.*, 2024, **10**, 100767.

27 V. T. Le, V. H. Hoang, H. Y. Hoang, A. T. Nguyen, V.-D. Doan and V. A. Tran, *Biomass Bioenergy*, 2025, **193**, 107554.

28 L. I. Ledesma-Fosados, N. V. Gallardo-Rivas, U. Páramo-García, R. García-Alamilla, J. d. J. Pérez-Bueno and

A. M. Mendoza-Martínez, *Int. J. Electrochem. Sci.*, 2025, **20**, 100956.

29 S. Adomaviciute-Grabusove, O. Bibikova, T. Sakharova, V. Artyushenko and V. Sablinskas, *ACS Appl. Nano Mater.*, 2025, **8**, 4252–4262.

30 S. Ben Ayed, L. Mansour, V. Vaiano, A. Halim Harrath, F. Ayari and L. Rizzo, *J. Photochem. Photobiol., A*, 2023, **438**, 114566.

31 J. Zheng, F. R. García-García, Y. Yang, K. Li, T. Bridgwater, H. Yang and Z. Wu, *Appl. Catal., B*, 2025, **366**, 125069.

32 F. Wang, M. Wang, D. Li and D. Yang, *Opt. Mater. Express*, 2012, **2**, 1437.

33 P. Jiang, K. Wang, W. Liu, Y. Song, R. Zheng, L. Chen and B. Su, *Polymers*, 2024, **16**, 2317.

34 X. Chen, M. Zhang, H. Qin, J. Zhou, Q. Shen, K. Wang, W. Chen, M. Liu and N. Li, *Sep. Purif. Technol.*, 2022, **280**, 119751.

35 J. Song, L. Zhu, S. Yu, G. Li and D. Wang, *RSC Adv.*, 2024, **14**, 33489–33511.

36 M. Golmohammadi, H. Hanafi-Bojd and M. Shiva, *Ceram. Int.*, 2023, **49**, 7717–7726.

37 C. Geng, Q. Chen, Z. Li, M. Liu, Z. Chen, H. Tao, Q. Yang, B. Zhu and L. Feng, *Environ. Res.*, 2023, **237**, 116960.

38 P. Huang and J. Luan, *RSC Adv.*, 2020, **10**, 4286–4292.

39 Z. H. Jabbar, B. H. Graimed, A. A. Okab, S. H. Ammar, M. A. Hussein and A. Majdi, *Sol. Energy*, 2025, **287**, 113216.

40 Q. Zhang, Y. Tan, Y. Chen, A. Xu and Y. Zhang, *Water Resour. Ind.*, 2024, **31**, 100257.

41 X.-J. Wen, C.-G. Niu, L. Zhang, C. Liang and G.-M. Zeng, *Appl. Catal., B*, 2018, **221**, 701–714.

42 H. Zhu, J. Yao, Z. Zhang, X. Jiang, Y. Zhou, Y. Bai, X. Hu, H. Ning and J. Hu, *J. Hazard. Mater.*, 2022, **434**, 128767.

43 M. J. Martínez-Mejía, I. Sato and S. Rath, *Environ. Sci. Pollut. Res.*, 2017, **24**, 15995–16006.

44 M. Rigoletto, E. Laurenti and M. L. Tummino, *Catalysts*, 2024, **14**, 267.

45 Z. Zheng, R. Shi, X. Zhang, Y. Ni and H. Zhang, *Polymers*, 2024, **16**, 1115.

46 R. Saleh and A. Taufik, *Environ. Nanotechnol., Monit. Manage.*, 2019, **11**, 100221.

47 X. Zhang, Z. Chen, X. Li, Y. Wu, J. Zheng, Y. Li, D. Wang, Q. Yang, A. Duan and Y. Fan, *Sep. Purif. Technol.*, 2023, **310**, 123116.

48 T. Wang, C. Zhao, L. Meng, Y. Li, D. Wang and C.-C. Wang, *Appl. Catal., B*, 2023, **334**, 122832.

49 X. Chen, Y. Zhang and J. Liu, *Int. Microbiol.*, 2024, **27**, 1693–1705.